



Second order method for solving 3D elasticity equations with complex interfaces



Bao Wang^a, Kelin Xia^a, Guo-Wei Wei^{a,b,c,*}

^a Department of Mathematics, Michigan State University, East Lansing, MI 48824, USA

^b Department of Electrical and Computer Engineering, Michigan State University, East Lansing, MI 48824, USA

^c Center for Mathematical Molecular Biosciences, Michigan State University, East Lansing, MI 48824, USA

ARTICLE INFO

Article history:

Received 1 August 2014

Received in revised form 17 February 2015

Accepted 28 March 2015

Available online 3 April 2015

Keywords:

Elasticity interface problem

Complex interface

Matched interface and boundary

ABSTRACT

Elastic materials are ubiquitous in nature and indispensable components in man-made devices and equipments. When a device or equipment involves composite or multiple elastic materials, elasticity interface problems come into play. The solution of three-dimensional (3D) elasticity interface problems is significantly more difficult than that of elliptic counterparts due to the coupled vector components and cross derivatives in the governing elasticity equations. This work introduces the matched interface and boundary (MIB) method for solving 3D elasticity interface problems. The proposed MIB elasticity interface scheme utilizes fictitious values on irregular grid points near the material interface to replace function values in the discretization so that the elasticity equation can be discretized using the standard finite difference schemes as if there were no material interface. The interface jump conditions are rigorously enforced on the intersecting points between the interface and the mesh lines. Such an enforcement determines the fictitious values. A number of new techniques have been developed to construct efficient MIB elasticity interface schemes for dealing with cross derivative in coupled governing equations. The proposed method is extensively validated over both weak and strong discontinuities of the solution, both piecewise constant and position-dependent material parameters, both smooth and nonsmooth interface geometries, and both small and large contrasts in the Poisson's ratio and shear modulus across the interface. Numerical experiments indicate that the present MIB method is of second order convergence in both L_∞ and L_2 error norms for handling arbitrarily complex interfaces, including biomolecular surfaces. To our best knowledge, this is the first elasticity interface method that is able to deliver the second convergence for the molecular surfaces of proteins.

© 2015 Elsevier Inc. All rights reserved.

1. Introduction

Although materials, such as solids, are composed of atoms or molecules, which are discrete in nature, continuum models based on the continuum mechanics are highly accurate and applicable to length scales much greater than that of interatomic distances [4]. One of the most widely applied continuum models is elasticity theory, which describes how solid materials return to their original shapes once being deformed by applied forces. Linear elasticity theory is often employed

* Corresponding author at: Department of Mathematics, Michigan State University, East Lansing, MI 48824, USA.

E-mail address: wei@math.msu.edu (G.-W. Wei).

when the deformation is relatively small. In such a case, the stress-strain relation is governed by the constitutive equation. One class of elastic materials is isotropic homogeneous, whose constitutive equations can be uniquely determined with any two terms of six moduli, namely, bulk modulus, Young's modulus, Lamé's first parameter, shear modulus, Poisson's ratio and p-wave modulus [1]. For isotropic inhomogeneous materials, the inhomogeneity is often modeled by position-dependent moduli in their constitutive equations. For example, in seismic wave equations, inhomogeneity is accounted by position-dependent Lamé's parameters [21]. Similar models have also been employed in the elasticity analysis of biomolecules [25–27].

Interface description in the elasticity modeling is indispensable whenever elastic materials encounter rapid changes or discontinuities in material properties due to voids, pores, inclusions, dislocations, cracks or composite structures [5,9,23,22]. The resulting problem is called an elasticity interface problem, which is of considerable importance in man-made materials, devices, equipments, tissue engineering, biomedical science and biophysics [23,22,25–27]. Mathematically, discontinuities in elasticity interface problems can be classified into two types, namely, strong ones and weak ones. Strong discontinuities are referred to situations where the displacement has jumps across the interface, while weak discontinuities have a continuous displacement but with jumps in the gradient of the displacement. In general, analytical solution to elasticity interface problems is difficult to obtain, except for simple interface geometries. In 1950s, Eshelby found that under a uniformly applied stress, an infinite and elastically isotropic system with an ellipsoidal inhomogeneity has a uniform eigenstrain distribution inside the ellipsoidal domain [6,7]. For arbitrarily shaped inhomogeneity, semianalytic approaches have been proposed for finding stress tensors [18].

Numerical approaches, such as finite element methods (FEMs), boundary element methods (BEMs) and finite difference methods (FDMs), are the main workhorse for elasticity interface problems arising from practical applications. Based on computational meshes used, these methods can be classified into two types, i.e., schemes utilize body-fitting meshes and algorithms based on special interface schemes. Body-fitting meshes are generated according to geometry of the interface so that no mesh lines cut through the interface. In this type of methods, locally adaptive meshes are frequently employed based on local refinement techniques [30]. In the second type of algorithms, regular meshes that may cut through the interface are used. Consequently, sophisticated numerical schemes are needed to incorporate the interface conditions into element shape functions or operator discretizations. Immersed interface method (IIM) originally proposed for elliptic interface problems [14] has been developed to solve two-dimensional (2D) elasticity interface problems with isotropic homogeneous media [31]. This finite difference based approach achieves second order accuracy. A second-order sharp numerical method has been developed for linear elasticity equations [24]. Many finite element based methods have also been proposed for elasticity interface problems. Among them, partition of unity method (PUM), the generalized finite element method (GFEM) and extended finite element method (XFEM) are designed to capture the non-smooth property of the solution over the interface [23,22,9]. Enrichment functions are utilized to handle the material interface. Discontinuous Galerkin based methods have also been constructed to deal with strong and weak discontinuities [12,2,19]. Recently, immersed finite element (IFEM) method has been developed to solve elasticity problems with interface jump conditions [15,29]. This approach locally modifies finite element basis functions to enforce the jump conditions across the interface. Most recently, a Nitsche type method has been proposed for elasticity interface problems [20].

There are few numerical issues in the solution of elasticity interface problems. One issue is to deal with complex interface geometry. It is easy to construct a numerical method for some special designed simple interface shapes. However, it is a challenge to automatically deal with complex interface geometries. Another issue is to develop robust numerical schemes for handling interfaces of Lipschitz continuity or geometric singularities, such as cusps, sharp edges, tips and self-intersecting surfaces [13]. It is still a major challenge to develop second order accurate schemes for arbitrarily complex interface geometries in a three-dimensional (3D) setting. One example of arbitrarily complex interface geometries is the protein molecular surfaces [32,33,11]. The other issue is position dependent material parameters. It is necessary for numerical methods to be able to treat spatially varying coefficients. Additionally, taking care of strong discontinuities, handling large contrast between material parameters across the interfaces and treatment of the Poisson's ratio near the incompressible limit are also valid numerical issues in elasticity interface problems [17,16]. Finally, it is a challenge to develop second order accurate schemes for arbitrarily complex interface geometries in three-dimensional (3D) setting. As a vector equation, the existence of three deformation components gives rise to an extraordinary requirement for numerical schemes to be unusually efficient. Although many elegant and efficient algorithms have been developed for 2D and 3D elasticity interface problems, to our best knowledge, there is little literature about second order convergent schemes for arbitrarily complex interface geometries in 3D, including interfaces of Lipschitz continuity.

The matched interface and boundary (MIB) method was originally constructed for dealing with material interfaces in Maxwell's equations [36] and Poisson equation [32,33,42,41,11]. The essential idea of the MIB method is to extend the solution beyond the interface so that the derivatives near the interface can be discretized as if there were no interface. The extension along the interface is carried out by iteratively incorporating the lowest order of interface conditions so that in principle, arbitrarily high order accuracy can be achieved. Sixteenth order accuracy was achieved for simple interface geometries [36,42] and up to sixth order convergence was realized for 3D complex interface shapes [33]. For arbitrarily complex interfaces with geometric singularities, robust second order numerical convergence was observed [32,33,11]. In the past decade, the MIB method has been successfully applied to a variety of problems. For example, in computational biophysics, an MIB based Poisson–Boltzmann solver, MIBPB [3], has been developed for the analysis of the electrostatic potential of biomolecules [32,11,39], molecular dynamics [10] and charge transport phenomenon [37,38]. Zhao has constructed second

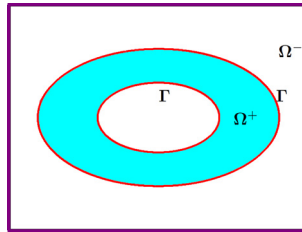


Fig. 1. Illustration of the elasticity interface problem at a cross section. The whole domain consists of two subdomains Ω^+ and Ω^- by the interface Γ .

order and fourth order MIB schemes for the Helmholtz problems [35,34]. A second order MIB method has been developed by Zhou and coworkers to solve the Navier–Stokes equations with discontinuous viscosity and density [40]. Recently, the MIB method has been extended to solve elliptic equations with multi-material interfaces [28].

The objective of the present work is to develop MIB schemes for solving 3D elasticity interface problems. We consider both smooth and sharp interfaces for isotropic homogeneous and inhomogeneous elastic materials. First, we extend our earlier MIB method for elliptic interface problems to elasticity counterparts. To this end, we take care of both central derivatives and cross derivatives in the elasticity equation. Several numerical techniques namely, disassociation, extrapolation, and neighbor combination, are proposed to compute the fictitious values for the discretization of the cross derivatives. Additionally, to make the present MIB method efficient for dealing with three coupled vector components, we carefully optimize our algorithms so that the resulting discretization matrix is as symmetric and diagonally dominant as possible. Moreover, to handle geometric singularities, we develop a technique to simultaneously employ two sets of interface conditions from two intersecting points where the interface meets mesh lines. Finally, we validate the proposed MIB for wide variety of elasticity interface problems, including large contrast in material parameters across the interface, strong interface discontinuity, sharp-edged interface, interface with variable material coefficients and biomolecular interfaces.

The rest of this paper is organized as follows. The formulation of 3D elasticity interface problems is presented in Section 2. Section 3 is devoted to the construction of MIB algorithms for elasticity interface problems. Methods for determining fictitious values are proposed for both central derivatives and cross derivatives in the elasticity equation. The present methods are extensively validated by analytical tests with complex interface geometries, including interfaces of Lipschitz continuity in Section 4. We demonstrate that the second order accuracy is achieved by the proposed MIB method. This paper ends with a conclusion.

2. Formulation of the elasticity interface problem

The 3D linear elasticity motion considered in the present work is governed by the following linear elasticity equations

$$\nabla \cdot \mathbb{T} + \mathbf{F} = \frac{d^2 \mathbf{u}}{dt^2}, \tag{1}$$

where \mathbb{T} is the strain tensor, $\mathbf{F} = (F_1(\mathbf{x}), F_2(\mathbf{x}), F_3(\mathbf{x}))^T := (F_1, F_2, F_3)^T$ is the external force on the elasticity body, $\mathbf{u} = (u_1(\mathbf{x}), u_2(\mathbf{x}), u_3(\mathbf{x}))^T$ is a displacement vector, $\mathbf{x} = (x, y, z)^T$ is a position vector, and $*^T$ is the transpose of quantity $*$.

For isotropic homogeneous media, the strain tensor \mathbb{T} is a 3 by 3 symmetric matrix which has the form

$$\mathbb{T} = \lambda \operatorname{tr}(\sigma) I + 2\mu \sigma, \tag{2}$$

where λ is the Lamé’s parameter, μ is the shear modulus, I is a 3 by 3 identity matrix, and σ is a stress tensor which can be further written as

$$\sigma = \frac{1}{2} (\nabla \mathbf{u} + (\nabla \mathbf{u})^T). \tag{3}$$

The static state elasticity equation is given by

$$\nabla \cdot \mathbb{T} + \mathbf{F} = \mathbf{0}. \tag{4}$$

In the present work, we focus on the static state problem (4).

2.1. Interface jump conditions

Consider a two-phase elastic body having two different elastic materials in a rectangular prism domain $\Omega \subset \mathbb{R}^3$. The two phase elastic motion is separated by an arbitrarily complex interface Γ , which splits the whole domain Ω into Ω^+ and Ω^- , i.e., $\Omega = \Omega^+ \cup \Gamma \cup \Omega^-$, as illustrated in Fig. 1.

Lemma 2.1. For the 3D elasticity equations of the static state (4), if the source term \mathbf{F} has a potential function representation U , i.e., $\nabla U = \mathbf{F}$, then the static state elasticity equations can be written as a homogeneous equation. More precisely, there exist another 3 by 3 matrix $\tilde{\mathbb{T}}$ such that

$$\nabla \cdot \tilde{\mathbb{T}} = \mathbf{0},$$

where $\mathbf{0}$ is the 3D zero vector.

Definition 2.1. Weak Solution: $\tilde{\mathbb{T}}$ is said to be the weak solution of the homogeneous equation $\nabla \cdot \tilde{\mathbb{T}} = \mathbf{0}$ provided

$$\int_{\Omega} \nabla \phi \cdot \tilde{\mathbb{T}} d\mathbf{r} = 0,$$

holds for $\forall \phi \in C_0^\infty(\Omega)$, where $C_0^\infty(\Omega)$ is the space of smooth functions with compact support on Ω , and $d\mathbf{r} = dx dy dz$ is the volume integral element.

Theorem 2.1. Let \mathbb{T} be a second order tensor in \mathbb{R}^3 which can be written as a 3 by 3 matrix. For the elasticity equations

$$\nabla \cdot \mathbb{T} + \mathbf{F} = \mathbf{0}, \tag{5}$$

where \mathbf{F} is a 3-dimensional vector valued function and $\mathbf{0} \in \mathbb{R}^3$. If the force term has a potential function U , i.e., $\nabla U = \mathbf{F}$, then across the interface, the weak solution satisfies the following interface conditions

$$[\mathbb{T} \cdot \mathbf{n}] = \mathbf{T}, \tag{6}$$

where \mathbf{T} is a 3-dimensional vector-valued function, $[*]$ is the jump of quantity $*$ across the interface, and \mathbf{n} is the normal direction of the interface.

Remark 1. If the material has no fracture which corresponds to the weak discontinuity in the linear elasticity interface problem, the following interface condition is enforced in traditionally elasticity interface problems

$$[\mathbf{u}] = \mathbf{0}.$$

However, fractures often occur in realistic materials which corresponds to the strong discontinuity. In this work, our numerical scheme is designed for both strong and weak discontinuity of elasticity interface problems.

2.2. Linear elasticity interface problem

In this work, we only consider the static state elasticity equation (4). As discussed above, the 3D elasticity interface problem can be formulated as

$$\nabla \cdot \mathbb{T} + \mathbf{F} = \mathbf{0}, \quad \text{in } \Omega^+ \cup \Omega^-, \tag{7}$$

$$[\mathbf{u}]|_{\Gamma} = \mathbf{b}, \quad \text{on } \Gamma, \tag{8}$$

$$[\mathbb{T} \cdot \mathbf{n}]|_{\Gamma} = \mathbf{T}, \quad \text{on } \Gamma, \tag{9}$$

$$\mathbf{u} = \mathbf{u}^0, \quad \text{on } \partial\Omega, \tag{10}$$

where $\mathbf{u} = (u_1, u_2, u_3)^T : \Omega \rightarrow \mathbb{R}^3$ is the displacement field and $\mathbf{n} = (n_1, n_2, n_3)^T$ is the unit outer normal vector to the interface Γ . Function \mathbf{F} , as stated above, is a 3D vector-valued function of body force field. Vector $\mathbf{u}^0 = (u_1^0, u_2^0, u_3^0)^T$ is the Dirichlet boundary conditions. For elasticity interface problem, generally, if vector $\mathbf{b} = (b_1, b_2, b_3)$ does not equal 0, it is called strong discontinuity, otherwise weak discontinuity. Here vector valued function $\mathbf{T} = (\phi, \psi, \eta)^T$ are the jump of the traction $\mathbb{T} \cdot \mathbf{n}$ across the interface Γ .

In material science, the stress-strain relation is usually described by constitutive equation, which in terms of Lamé’s parameters can be expressed as,

$$\mathbb{T} = \lambda \text{tr}(\sigma)I + 2\mu\sigma. \tag{11}$$

Here strain tensor σ is defined as,

$$\sigma = \frac{1}{2} \left(\nabla \mathbf{u} + (\nabla \mathbf{u})^T \right).$$

Dramatically different elasticity behaviors can be observed between inhomogeneous media and homogeneous media. To take this property into consideration, we elaborate the elasticity interface problem in both situations. For inhomogeneous material, Lamé’s parameters are position dependent, i.e., $\lambda = \lambda(x, y, z)$ and $\mu = \mu(x, y, z)$. Using the constitutive relation in Eq. (11), the governing equation of elasticity interface problem can be expressed as,

$$\nabla \lambda (\nabla \cdot \mathbf{u}) + \nabla \mu \cdot \left[\nabla \mathbf{u} + (\nabla \mathbf{u})^T \right] + (\lambda + \mu) \nabla \nabla \cdot \mathbf{u} + \mu \nabla^2 \mathbf{u} = -\mathbf{F}. \tag{12}$$

We can spell out all the terms as follows:

$$\begin{aligned}
 &(\lambda + 2\mu)\frac{\partial^2 u_1}{\partial x^2} + \mu\frac{\partial^2 u_1}{\partial y^2} + \mu\frac{\partial^2 u_1}{\partial z^2} + (\lambda + \mu)\frac{\partial^2 u_2}{\partial x\partial y} + (\lambda + \mu)\frac{\partial^2 u_3}{\partial x\partial z} + \lambda_x\left(\frac{\partial u_1}{\partial x} + \frac{\partial u_2}{\partial y} + \frac{\partial u_3}{\partial z}\right) \\
 &+ 2\mu_x\frac{\partial u_1}{\partial x} + \mu_y\left(\frac{\partial u_1}{\partial y} + \frac{\partial u_2}{\partial x}\right) + \mu_z\left(\frac{\partial u_1}{\partial z} + \frac{\partial u_3}{\partial x}\right) = -F_1,
 \end{aligned} \tag{13}$$

$$\begin{aligned}
 &\mu\frac{\partial^2 u_2}{\partial x^2} + (\lambda + 2\mu)\frac{\partial^2 u_2}{\partial y^2} + \mu\frac{\partial^2 u_2}{\partial z^2} + (\lambda + \mu)\frac{\partial^2 u_1}{\partial x\partial y} + (\lambda + \mu)\frac{\partial^2 u_3}{\partial y\partial z} + \mu_x\left(\frac{\partial u_2}{\partial x} + \frac{\partial u_1}{\partial y}\right) \\
 &+ \lambda_y\left(\frac{\partial u_1}{\partial x} + \frac{\partial u_2}{\partial y} + \frac{\partial u_3}{\partial z}\right) + 2\mu_y\frac{\partial u_2}{\partial y} + \mu_z\left(\frac{\partial u_2}{\partial z} + \frac{\partial u_3}{\partial y}\right) = -F_2,
 \end{aligned} \tag{14}$$

$$\begin{aligned}
 &\mu\frac{\partial^2 u_3}{\partial x^2} + \mu\frac{\partial^2 u_3}{\partial y^2} + (\lambda + 2\mu)\frac{\partial^2 u_3}{\partial z^2} + (\lambda + \mu)\frac{\partial^2 u_1}{\partial x\partial z} + (\lambda + \mu)\frac{\partial^2 u_2}{\partial y\partial z} + \mu_x\left(\frac{\partial u_3}{\partial x} + \frac{\partial u_1}{\partial z}\right) + \mu_y\left(\frac{\partial u_3}{\partial y} + \frac{\partial u_2}{\partial z}\right) \\
 &+ \lambda_z\left(\frac{\partial u_1}{\partial x} + \frac{\partial u_2}{\partial y} + \frac{\partial u_3}{\partial z}\right) + 2\mu_z\frac{\partial u_3}{\partial z} = -F_3.
 \end{aligned} \tag{15}$$

With the constitutive equations, the jump conditions regarding to the strain tensor can be represented as,

$$\left[\left(\lambda \left(\frac{\partial u_1}{\partial x} + \frac{\partial u_2}{\partial y} + \frac{\partial u_3}{\partial z} \right) + 2\mu \frac{\partial u_1}{\partial x} \right) n_1 + \mu \left(\frac{\partial u_2}{\partial x} + \frac{\partial u_1}{\partial y} \right) n_2 + \mu \left(\frac{\partial u_3}{\partial x} + \frac{\partial u_1}{\partial z} \right) n_3 \right]_{\Gamma} = \phi, \text{ on } \Gamma, \tag{16}$$

$$\left[\mu \left(\frac{\partial u_1}{\partial y} + \frac{\partial u_2}{\partial x} \right) n_1 + \left(\lambda \left(\frac{\partial u_1}{\partial x} + \frac{\partial u_2}{\partial y} + \frac{\partial u_3}{\partial z} \right) + 2\mu \frac{\partial u_2}{\partial y} \right) n_2 + \mu \left(\frac{\partial u_3}{\partial y} + \frac{\partial u_2}{\partial z} \right) n_3 \right]_{\Gamma} = \psi, \text{ on } \Gamma, \tag{17}$$

$$\left[\mu \left(\frac{\partial u_1}{\partial z} + \frac{\partial u_3}{\partial x} \right) n_1 + \mu \left(\frac{\partial u_2}{\partial z} + \frac{\partial u_3}{\partial y} \right) n_2 + \left(\lambda \left(\frac{\partial u_1}{\partial x} + \frac{\partial u_2}{\partial y} + \frac{\partial u_3}{\partial z} \right) + 2\mu \frac{\partial u_3}{\partial z} \right) n_3 \right]_{\Gamma} = \eta, \text{ on } \Gamma. \tag{18}$$

Together with the Dirichlet boundary conditions and the jump conditions, we set up the general formulation for linear elasticity interface problem with inhomogeneous media.

For homogeneous material, algebraic relations exist between different elasticity moduli, i.e., Bulk modulus K , Young's modulus E , Lamé's first parameter λ , shear modulus μ , Poisson's ratio ν and P-wave modulus M . For instance, Lamé's parameters can be represented by Young's modulus E and Poisson's ratio ν as,

$$\mu = \frac{E}{2(1 + \nu)}, \quad \lambda = \frac{E\nu}{(1 + \nu)(1 - 2\nu)}.$$

Due to the constant moduli, the governing equation can be simplified as

$$(\lambda + \mu)\nabla\nabla \cdot \mathbf{u} + \mu\nabla^2 \mathbf{u} = -\mathbf{F}. \tag{19}$$

With the above algebraic relations of elasticity moduli, the governing equation can be further written as,

$$2(1 - \nu)\frac{\partial^2 u_1}{\partial x^2} + (1 - 2\nu)\frac{\partial^2 u_1}{\partial y^2} + (1 - 2\nu)\frac{\partial^2 u_1}{\partial z^2} + \frac{\partial^2 u_2}{\partial x\partial y} + \frac{\partial^2 u_3}{\partial x\partial z} = f_1, \tag{20}$$

$$(1 - 2\nu)\frac{\partial^2 u_2}{\partial x^2} + 2(1 - \nu)\frac{\partial^2 u_2}{\partial y^2} + (1 - 2\nu)\frac{\partial^2 u_2}{\partial z^2} + \frac{\partial^2 u_1}{\partial x\partial y} + \frac{\partial^2 u_3}{\partial y\partial z} = f_2, \tag{21}$$

$$(1 - 2\nu)\frac{\partial^2 u_3}{\partial x^2} + (1 - 2\nu)\frac{\partial^2 u_3}{\partial y^2} + 2(1 - \nu)\frac{\partial^2 u_3}{\partial z^2} + \frac{\partial^2 u_1}{\partial x\partial z} + \frac{\partial^2 u_2}{\partial y\partial z} = f_3. \tag{22}$$

Here (f_1, f_2, f_3) are prerequisite terms, and they can be related to the body force by $(f_1, f_2, f_3) = \left(-\frac{F_1}{\mu+\lambda}, -\frac{F_2}{\mu+\lambda}, -\frac{F_3}{\mu+\lambda}\right)$.

Also the second set of jump conditions can be rewritten as,

$$\left[\frac{2\mu}{1 - 2\nu} \left((1 - \nu)\frac{\partial u_1}{\partial x} + \nu\frac{\partial u_2}{\partial y} + \nu\frac{\partial u_3}{\partial z} \right) n_1 + \mu \left(\frac{\partial u_1}{\partial y} + \frac{\partial u_2}{\partial x} \right) n_2 + \mu \left(\frac{\partial u_1}{\partial z} + \frac{\partial u_3}{\partial x} \right) n_3 \right]_{\Gamma} = \phi, \text{ on } \Gamma, \tag{23}$$

$$\left[\mu \left(\frac{\partial u_1}{\partial y} + \frac{\partial u_2}{\partial x} \right) n_1 + \frac{2\mu}{1 - 2\nu} \left(\nu\frac{\partial u_1}{\partial x} + (1 - \nu)\frac{\partial u_2}{\partial y} + \nu\frac{\partial u_3}{\partial z} \right) n_2 + \mu \left(\frac{\partial u_3}{\partial y} + \frac{\partial u_2}{\partial z} \right) n_3 \right]_{\Gamma} = \psi, \text{ on } \Gamma, \tag{24}$$

$$\left[\mu \left(\frac{\partial u_1}{\partial z} + \frac{\partial u_3}{\partial x} \right) n_1 + \mu \left(\frac{\partial u_2}{\partial z} + \frac{\partial u_3}{\partial y} \right) n_2 + \frac{2\mu}{1 - 2\nu} \left(\nu\frac{\partial u_1}{\partial x} + \nu\frac{\partial u_2}{\partial y} + (1 - \nu)\frac{\partial u_3}{\partial z} \right) n_3 \right]_{\Gamma} = \rho, \text{ on } \Gamma. \tag{25}$$

The above two sets of equations, together with the Dirichlet boundary conditions and jump conditions regarding to displacement, constitute general formulation for linear elasticity interface problem in homogeneous media.

3. Method and algorithm

In this section, the MIB method for elliptical interface problems is extended to solve elasticity interface problems. Due to the existence of the interface, the direct application of the standard central finite difference (CFD) schemes leads to a dramatic decrease in the accuracy and convergence of the numerical solution. To maintain the designed order of accuracy, MIB method extends function values across the interface. The resulting extended function values are called fictitious values, which are employed, together with function values on the other side of the interface, for the CFD discretization of the PDE across the interface. For example, at a grid point (i, j, k) near the interface, if its finite difference scheme refers to some grid points that are in the other side of the interface, fictitious values from other side of the interface are utilized in the finite difference discretization. To extend the function values to the other side of the interface and enable the MIB discretization of second order convergence, the interface conditions on both function values and normal derivatives are utilized and enforced.

The location of a fictitious value is called an irregular grid point, while those grid points where no fictitious value is required are called regular grid points. Loosely speaking, irregular grid points form extended domains on both sides of the interface. The extended domains ensure that the standard central finite difference scheme can be uniformly applied without the loss of numerical accuracy.

Additionally, derivatives involved in the elasticity equation are classified into central derivatives and cross derivatives. Central derivatives involve only one direction, while cross derivatives refer to more than one direction. These two situations are to be handled in different manners in the present method. Additional care is needed for discretizing cross derivatives to the second order accuracy.

Moreover, interfaces are classified into smooth ones and nonsmooth ones. The nonsmooth interfaces are Lipschitz continuous with geometric singularities, such as cusps, tips and/or sharp edges. To maintain designed order of accuracy, nonsmooth interfaces are much more difficult to deal with.

3.1. General MIB algorithms for Laplace operator

3.1.1. Simplification of interface jump conditions

As the interface normal direction varies along the interface, which is very troublesome from a computational perspective. It is necessary to define a set of local coordinates at each intersection point of the interface and the Cartesian mesh, so that different interface geometries can be treated in a systematical manner. In this section, we present the local coordinate transformation formula. At a specific intersection point, the local coordinate system is chosen to be (ξ, η, ζ) , where ξ is along the normal direction and η is in the xy plane. This local coordinate system can be obtained from the Cartesian coordinate system via the following transformation

$$\begin{pmatrix} \xi \\ \eta \\ \zeta \end{pmatrix} = \mathbf{P} \cdot \begin{pmatrix} x \\ y \\ z \end{pmatrix}, \quad (26)$$

where $\mathbf{P} \doteq \{P(i, j)\}_{i,j=1,2,3}$ is a transformation matrix

$$\mathbf{P} = \begin{pmatrix} \sin \phi \cos \theta & \sin \phi \sin \theta & \cos \phi \\ -\sin \theta & \cos \theta & 0 \\ -\cos \phi \cos \theta & -\cos \phi \sin \theta & \sin \phi \end{pmatrix}, \quad (27)$$

where θ and ϕ are the azimuth and zenith angle with respect to the normal direction, respectively.

In the new local coordinate system, the interface conditions on function values and normal derivatives become (here for simplicity, we only discuss the constant material parameter case, the case of spatially dependent material parameters can be treated similarly)

$$[\mathbf{u}]|_{\Gamma} = \mathbf{b}, \quad (28)$$

and

$$[\mathbb{T} \cdot \xi]|_{\Gamma} = \mathbf{T}. \quad (29)$$

To achieve better stability and higher efficiency, which is essential for the present 3D vector equation, only the lowest order jump conditions are utilized in the MIB method. Therefore, we avoid generating high order (derivative) jump conditions, even if in arbitrarily high order MIB methods [36,42,32]. However, we hope to have as many low order jump conditions as possible so as to gain flexibility in dealing with complex interface geometries. To this end, we differentiate the jump condition of the vector function to derive two additional sets of interface jump conditions along η and ζ directions, respectively

$$[\mathbf{u}_{,\eta}]|_{\Gamma} = \left(-\sin \theta \frac{\partial \mathbf{u}^+}{\partial x} + \cos \theta \frac{\partial \mathbf{u}^+}{\partial y} \right) - \left(-\sin \theta \frac{\partial \mathbf{u}^-}{\partial x} + \cos \theta \frac{\partial \mathbf{u}^-}{\partial y} \right), \quad (30)$$

and

$$[\mathbf{u}_\zeta]|\Gamma = \left(-\cos\phi \cos\theta \frac{\partial \mathbf{u}^+}{\partial x} - \cos\phi \sin\theta \frac{\partial \mathbf{u}^+}{\partial y} + \sin\phi \frac{\partial \mathbf{u}^+}{\partial z} \right) - \left(-\cos\phi \cos\theta \frac{\partial \mathbf{u}^-}{\partial x} - \cos\phi \sin\theta \frac{\partial \mathbf{u}^-}{\partial y} + \sin\phi \frac{\partial \mathbf{u}^-}{\partial z} \right), \tag{31}$$

where $\mathbf{u} = (u_1, u_2, u_3)^T$.

In summary, at a specific intersection point of the interface and the mesh line, there are four sets of interface conditions (28)–(31), which only refer to the function values and lowest order derivatives. This property is crucial to endow the MIB method with high efficiency and stability in handling complex interface geometries since no higher order derivative is referred in determining fictitious values. Additionally, lowest order derivatives lead to a more banded matrix and a smaller condition number, which are crucial in solving 3D vector interface problems.

In the MIB method, the function values near the interface are extended across the interface by introducing fictitious values. The extension is done along one mesh line at a time, so that it is locally a 1D-like scheme for a higher-dimensional interface. Fictitious values can be determined by the aforementioned interface conditions (28)–(31). These conditions involve eighteen derivatives $\frac{\partial \mathbf{u}^\pm}{\partial x_j}$, where $x_j = x, y, z$ and $\mathbf{u} = (u_1, u_2, u_3)^T$. These derivatives are to be evaluated on the interface and thus are called interfacial derivatives. They are elements of a special interfacial vector α in our jump condition representation formulas (32). Due to the geometric complexity, some of these eighteen interfacial derivatives can be very difficult to compute numerically. In general, these interfacial derivatives are grouped into six sets because u_1, u_2 and u_3 can be treated in a similar manner in most situations.

In a second order scheme, we typically have two (sets of) fictitious values along one specific mesh line at one time. However, there are four sets of interface conditions. Therefore, two sets of interface conditions are redundant. This redundancy gives two more degrees of freedom for us to design efficient and robust second order schemes in a complex interface geometry. Our basic idea is to algebraically eliminate two sets of interfacial derivatives that are the most difficult to compute by using two sets of redundant interface conditions. Therefore, at each intersection point we only need to evaluate four sets of derivatives that are relatively easy to approximate numerically.

The two sets of derivatives that are to be eliminated are selected by the following principles.

- Two sets of fictitious values along the mesh line that intersects with the interface are determined at one time.
- Two sets of derivatives along the mesh line that intersect with the interface must be kept.
- In the remaining four sets of derivatives, select two sets that are most difficult to evaluate due to the local geometry and eliminate them by two sets of jump conditions.

Denote $\mathbf{T} := (T_1, T_2, T_3)^T$ in interface conditions (29), and by further introducing the matrix notation, the interface conditions (29)–(31) can be rewritten as:

$$\begin{aligned} & \left(T_1, T_2, T_3, \left[\frac{\partial u_1}{\partial \eta} \right], \left[\frac{\partial u_2}{\partial \eta} \right], \left[\frac{\partial u_3}{\partial \eta} \right], \left[\frac{\partial u_1}{\partial \zeta} \right], \left[\frac{\partial u_2}{\partial \zeta} \right], \left[\frac{\partial u_3}{\partial \zeta} \right] \right)^T \\ &= \mathbf{C} \left(\frac{\partial u_1^+}{\partial x}, \frac{\partial u_1^-}{\partial x}, \frac{\partial u_1^+}{\partial y}, \frac{\partial u_1^-}{\partial y}, \frac{\partial u_1^+}{\partial z}, \frac{\partial u_1^-}{\partial z}, \frac{\partial u_2^+}{\partial x}, \frac{\partial u_2^-}{\partial x}, \frac{\partial u_2^+}{\partial y}, \frac{\partial u_2^-}{\partial y}, \frac{\partial u_2^+}{\partial z}, \frac{\partial u_2^-}{\partial z}, \frac{\partial u_3^+}{\partial x}, \frac{\partial u_3^-}{\partial x}, \frac{\partial u_3^+}{\partial y}, \frac{\partial u_3^-}{\partial y}, \frac{\partial u_3^+}{\partial z}, \frac{\partial u_3^-}{\partial z} \right)^T \\ &\doteq \mathbf{C} \cdot \alpha \end{aligned} \tag{32}$$

where

$$\begin{aligned} \mathbf{C} &= \begin{pmatrix} C_{1,1} & C_{1,2} & C_{1,3} \\ C_{2,1} & C_{2,2} & C_{2,3} \\ C_{3,1} & C_{3,2} & C_{3,3} \end{pmatrix}, \\ C_{1,1} &= \begin{pmatrix} M^+P(1,1) & -M^-P(1,1) & \mu^+P(1,2) & -\mu^-P(1,2) & \mu^+P(1,3) & -\mu^-P(1,3) \\ \lambda^+P(1,2) & -\lambda^-P(1,2) & \mu^+P(1,1) & -\mu^-P(1,1) & 0 & 0 \\ \lambda^+P(1,3) & -\lambda^-P(1,3) & 0 & 0 & \mu^+P(1,1) & -\mu^-P(1,1) \end{pmatrix} \\ C_{1,2} &= \begin{pmatrix} \mu^+P(1,2) & -\mu^-P(1,2) & \lambda^+P(1,1) & -\lambda^-P(1,1) & 0 & 0 \\ \mu^+P(1,1) & -\mu^-P(1,1) & M^+P(1,2) & -M^-P(1,2) & \mu^+P(1,3) & -\mu^-P(1,3) \\ 0 & 0 & \lambda^+P(1,3) & -\lambda^-P(1,3) & \mu^+P(1,2) & -\mu^-P(1,2) \end{pmatrix} \\ C_{1,3} &= \begin{pmatrix} \mu^+P(1,3) & -\mu^-P(1,3) & 0 & 0 & \lambda^+P(1,1) & \lambda^-P(1,1) \\ 0 & 0 & \mu^+P(1,3) & -\mu^-P(1,3) & \lambda^+P(1,2) & -\lambda^-P(1,2) \\ \mu^+P(1,1) & -\mu^-P(1,1) & \mu^+P(1,2) & -\mu^-P(1,2) & M^+P(1,3) & -M^-P(1,3) \end{pmatrix} \end{aligned}$$

$$C_{2,1} = \begin{pmatrix} P(2,1) & -P(2,1) & P(2,2) & -P(2,2) & 0 & 0 \\ 0 & 0 & 0 & 0 & 0 & 0 \\ 0 & 0 & 0 & 0 & 0 & 0 \end{pmatrix}$$

$$C_{2,2} = \begin{pmatrix} 0 & 0 & 0 & 0 & 0 & 0 \\ P(2,1) & -P(2,1) & P(2,2) & -P(2,2) & 0 & 0 \\ 0 & 0 & 0 & 0 & 0 & 0 \end{pmatrix}$$

$$C_{2,3} = \begin{pmatrix} 0 & 0 & 0 & 0 & 0 & 0 \\ 0 & 0 & 0 & 0 & 0 & 0 \\ P(2,1) & -P(2,1) & P(2,2) & -P(2,2) & 0 & 0 \end{pmatrix}$$

$$C_{3,1} = \begin{pmatrix} P(3,1) & -P(3,1) & P(3,2) & -P(3,2) & P(3,3) & -P(3,3) \\ 0 & 0 & 0 & 0 & 0 & 0 \\ 0 & 0 & 0 & 0 & 0 & 0 \end{pmatrix}$$

$$C_{3,2} = \begin{pmatrix} 0 & 0 & 0 & 0 & 0 & 0 \\ P(3,1) & -P(3,1) & P(3,2) & -P(3,2) & P(3,3) & -P(3,3) \\ 0 & 0 & 0 & 0 & 0 & 0 \end{pmatrix}$$

$$C_{3,3} = \begin{pmatrix} 0 & 0 & 0 & 0 & 0 & 0 \\ 0 & 0 & 0 & 0 & 0 & 0 \\ P(3,1) & -P(3,1) & P(3,2) & -P(3,2) & P(3,3) & -P(3,3) \end{pmatrix}.$$

In the above expressions, $M = \frac{2\mu(1-\nu)}{1-2\nu}$, λ and μ are the p -wave module, bulk modulus and shear modulus, respectively. Here $*^+$ and $*^-$ are the limiting values of the quantity $*$ inside and outside the interface, respectively.

Lemma 3.1. Consider the matrix:

$$A \doteq \begin{pmatrix} M^+P(1,1) & -M^-P(1,1) & \mu^+P(1,2) & -\mu^-P(1,2) & \mu^+P(1,3) & -\mu^-P(1,3) \\ P(2,1) & -P(2,1) & P(2,2) & -P(2,2) & 0 & 0 \\ P(3,1) & -P(3,1) & P(3,2) & -P(3,2) & P(3,3) & -P(3,3) \end{pmatrix}$$

where M^+ , M^- , μ^+ , μ^- , $P(i, j)$, $i, j = 1, 2, 3$ are the same as above. Then $\forall 1 \leq l, m \leq 6, l \neq m$, there exists constants a, b, c such that the l -th and m -th column of the vector $aA(1, :) + bA(2, :) + cA(3, :)$ are both zero, where $A(1, :)$, $A(2, :)$, $A(3, :)$ are the first, second and the last row of the matrix A .

Proof. If $l = 5, m = 6$ or $l = 6, m = 5$ we simply let $a = 0, b = 1, c = 0$ then it is obvious that the 5-th and 6-th column of the vector $aA(1, :) + bA(2, :) + cA(3, :)$ are both zero.

Otherwise, we let:

$$a = A(2, l)A(3, m) - A(3, l)A(2, m),$$

$$b = A(3, l)A(1, m) - A(1, l)A(3, m),$$

$$c = A(1, l)A(2, m) - A(2, l)A(1, m),$$

then we have the l -th and m -th column of the vector $aA(1, :) + bA(2, :) + cA(3, :)$ are both zero. \square

Now suppose that according to the local geometry the l -th and m -th elements of the array:

$$\left(\frac{\partial \mathbf{u}^+}{\partial x}, \frac{\partial \mathbf{u}^-}{\partial x}, \frac{\partial \mathbf{u}^+}{\partial y}, \frac{\partial \mathbf{u}^-}{\partial y}, \frac{\partial \mathbf{u}^+}{\partial z}, \frac{\partial \mathbf{u}^-}{\partial z} \right), \quad (33)$$

are to be eliminated, where $1 \leq l, m \leq 6, l \neq m$. We are going to seek the combined interface conditions for computing the two pairs of fictitious values at the two irregular grid points.

First, if $l = 5, m = 6$ or $l = 6, m = 5$ then we simply employ the interface conditions (28) and (30) for computing the fictitious values. Otherwise, we have the following results.

Lemma 3.2. For given $1 \leq l, m \leq 6, l \neq 5$ or 6 , or $m \neq 5$ or 6 , then there exists constants $a_i, b_i, c_i, d_i, e_i, f_i, g_i, i = 1, 2, 3$, such that the l -th, m -th ($l+6$)-th ($m+6$)-th ($l+12$)-th and ($m+12$)-th elements of the following vectors are all zero:

$$\begin{aligned}
 & a_1C(1, :) + b_1C(4, :) + c_1C(7, :) + d_1C(5, :) + e_1C(8, :) + f_1C(6, :) + g_1C(9, :), \\
 & a_2C(2, :) + b_2C(4, :) + c_2C(7, :) + d_2C(5, :) + e_2C(8, :) + f_2C(6, :) + g_2C(9, :), \\
 & a_3C(3, :) + b_3C(4, :) + c_3C(7, :) + d_3C(5, :) + e_3C(8, :) + f_3C(6, :) + g_3C(9, :),
 \end{aligned}$$

where $C(i, :)$, $i = 1, \dots, 9$, is the i -th column of the above matrix C .

Proof. We only show that there exists constants $a_1, b_1, c_1, d_1, e_1, f_1, g_1$ such that the results stated in the lemma are true for the first vector, and the other two are the same.

Consider the following three matrices:

$$A_1 \doteq \begin{pmatrix} M^+P(1, 1) & -M^-P(1, 1) & \mu^+P(1, 2) & -\mu^-P(1, 2) & \mu^+P(1, 3) & -\mu^-P(1, 3) \\ P(2, 1) & -P(2, 1) & P(2, 2) & -P(2, 2) & 0 & 0 \\ P(3, 1) & -P(3, 1) & P(3, 2) & -P(3, 2) & P(3, 3) & -P(3, 3) \end{pmatrix}$$

$$A_2 \doteq \begin{pmatrix} \mu^+P(1, 2) & -\mu^-P(1, 2) & \lambda^+P(1, 1) & -\lambda^-P(1, 1) & 0 & 0 \\ P(2, 1) & -P(2, 1) & P(2, 2) & -P(2, 2) & 0 & 0 \\ P(3, 1) & -P(3, 1) & P(3, 2) & -P(3, 2) & P(3, 3) & -P(3, 3) \end{pmatrix}$$

$$A_3 \doteq \begin{pmatrix} \mu^+P(1, 3) & -\mu^-P(1, 3) & 0 & 0 & \lambda^+P(1, 1) & -\lambda^-P(1, 1) \\ P(2, 1) & -P(2, 1) & P(2, 2) & -P(2, 2) & 0 & 0 \\ P(3, 1) & -P(3, 1) & P(3, 2) & -P(3, 2) & P(3, 3) & -P(3, 3) \end{pmatrix}$$

According to the previous lemma, let

$$\begin{aligned}
 a_1 &= A_1(2, l)A_1(3, m) - A_1(3, l)A_1(2, m) = A_2(2, l)A_2(3, m) - A_2(3, l)A_2(2, m) \\
 &= A_3(2, l)A_3(3, m) - A_3(3, l)A_3(2, m) = C(4, l)C(7, m) - C(7, l)C(4, m), \\
 b_1 &= A_1(3, l)A_1(1, m) - A_1(1, l)A_1(3, m) = C(7, l)C(1, m) - C(1, l)C(7, m), \\
 c_1 &= A_1(1, l)A_1(2, m) - A_1(2, l)A_1(1, m) = C(1, l)C(4, m) - C(4, l)C(1, m), \\
 d_1 &= A_2(3, l)A_2(1, m) - A_2(1, l)A_2(3, m) = C(8, l+6)C(1, m+6) - C(1, l+6)C(8, m+6), \\
 e_1 &= A_2(1, l)A_2(2, m) - A_2(2, l)A_2(1, m) = C(1, l+6)C(5, m+6) - C(5, l+6)C(1, m+6), \\
 f_1 &= A_3(3, l)A_3(1, m) - A_3(1, l)A_3(3, m) = C(9, l+12)C(1, m+12) - C(1, l+12)C(9, m+12), \\
 g_1 &= A_3(1, l)A_3(2, m) - A_3(2, l)A_3(1, m) = C(1, l+12)C(6, m+12) - C(6, l+12)C(1, m+12),
 \end{aligned}$$

then we have the l -th and m -th column of the following vectors are all zero:

$$\begin{aligned}
 & a_1A_1(1, :) + b_1A_1(2, :) + c_1A_1(3, :), \\
 & a_1A_2(1, :) + d_1A_2(2, :) + e_1A_2(3, :), \\
 & a_1A_3(1, :) + f_1A_3(2, :) + g_1A_3(3, :).
 \end{aligned}$$

Note the relationship of the matrix C and the matrices A_1, A_2 and A_3 , it ends up that the l -th, m -th $(l+6)$ -th $(m+6)$ -th $(l+12)$ -th and $(m+12)$ -th elements of the following vector are all zero:

$$a_1C(1, :) + b_1C(4, :) + c_1C(7, :) + d_1C(5, :) + e_1C(8, :) + f_1C(6, :) + g_1C(9, :). \quad \square$$

According to the above lemma, if $l \neq 5$ or 6 , or, $m \neq 5$ or 6 . The following two sets of interface conditions can be employed to compute the fictitious values, which do not contains the l -th and m -th columns' elements of (33).

The first set of interface conditions is due to the jump of function values, i.e.,

$$[u_1]|_\Gamma = b_1, \tag{34}$$

$$[u_2]|_\Gamma = b_2, \tag{35}$$

$$[u_3]|_\Gamma = b_3. \tag{36}$$

The other set is due to derivatives,

$$\begin{aligned}
 & a_1T_1 + b_1\left[\frac{\partial u_1}{\partial \eta}\right] + c_1\left[\frac{\partial u_1}{\partial \zeta}\right] + d_1\left[\frac{\partial u_2}{\partial \eta}\right] + e_1\left[\frac{\partial u_2}{\partial \zeta}\right] + f_1\left[\frac{\partial u_3}{\partial \eta}\right] + g_1\left[\frac{\partial u_3}{\partial \zeta}\right] \\
 &= (a_1C(1, :) + b_1C(4, :) + c_1C(7, :) + d_1C(5, :) + e_1C(8, :) + f_1C(6, :) + g_1C(9, :)) \cdot \alpha,
 \end{aligned} \tag{37}$$

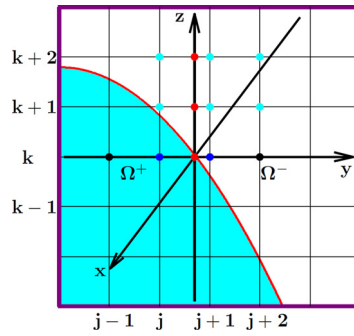


Fig. 2. Illustration of a smooth interface at cross section ($x = x_i$). The k -th mesh line along the y -direction intersects the interface at point (x_0, y_0, z_0) . A pair of fictitious values at irregular grid points (i, j, k) and $(i, j + 1, k)$ in blue color is to be determined. To this end function values and derivatives at (x_0, y_0, z_0) approximated from Ω^+ and Ω^- are to be matched. Four points along the y -direction are utilized to approximate quantities at (x_0, y_0, z_0) , and six cyan points are adopted to approximate $\frac{\partial \mathbf{u}^-(x_0, y_0, z_0)}{\partial z}$. (For interpretation of the references to color in this figure legend, the reader is referred to the web version of this article.)

$$\begin{aligned}
 a_2 T_2 + b_2 \left[\frac{\partial u_1}{\partial \eta} \right] + c_2 \left[\frac{\partial u_1}{\partial \zeta} \right] + d_2 \left[\frac{\partial u_2}{\partial \eta} \right] + e_2 \left[\frac{\partial u_2}{\partial \zeta} \right] + f_2 \left[\frac{\partial u_3}{\partial \eta} \right] + g_2 \left[\frac{\partial u_3}{\partial \zeta} \right] \\
 = (a_2 C(2, :) + b_2 C(4, :) + c_2 C(7, :) + d_2 C(5, :) + e_2 C(8, :) + f_2 C(6, :) + g_2 C(9, :)) \cdot \alpha,
 \end{aligned} \tag{38}$$

$$\begin{aligned}
 a_3 T_3 + b_3 \left[\frac{\partial u_1}{\partial \eta} \right] + c_3 \left[\frac{\partial u_1}{\partial \zeta} \right] + d_3 \left[\frac{\partial u_2}{\partial \eta} \right] + e_3 \left[\frac{\partial u_2}{\partial \zeta} \right] + f_3 \left[\frac{\partial u_3}{\partial \eta} \right] + g_3 \left[\frac{\partial u_3}{\partial \zeta} \right] \\
 = (a_3 C(3, :) + b_3 C(4, :) + c_3 C(7, :) + d_3 C(5, :) + e_3 C(8, :) + f_3 C(6, :) + g_3 C(9, :)) \cdot \alpha,
 \end{aligned} \tag{39}$$

where $a_1 = a_2 = a_3 = C(4, l)C(7, m) - C(7, l)C(4, m)$,

$$b_1 = C(7, l)C(1, m) - C(1, l)C(7, m),$$

$$c_1 = C(1, l)C(4, m) - C(4, l)C(1, m),$$

$$d_1 = C(8, l + 6)C(1, m + 6) - C(1, l + 6)C(8, m + 6),$$

$$e_1 = C(1, l + 6)C(5, m + 6) - C(5, l + 6)C(1, m + 6),$$

$$f_1 = C(9, 1 + 12)C(1, m + 12) - C(1, l + 12)C(9, m + 12),$$

$$g_1 = C(1, l + 12)C(6, m_1 2) - C(6, l + 12)C(1, m + 12),$$

$$b_2 = C(7, l)C(2, m) - C(2, l)C(7, m),$$

$$c_2 = C(2, l)C(4, m) - C(4, l)C(2, m),$$

$$d_2 = C(8, l + 6)C(2, m + 6) - C(2, l + 6)C(8, m + 6),$$

$$e_2 = C(2, l + 6)C(5, m + 6) - C(5, l + 6)C(2, m + 6),$$

$$f_2 = C(9, 1 + 12)C(2, m + 12) - C(2, l + 12)C(9, m + 12),$$

$$g_2 = C(2, l + 12)C(6, m + 12) - C(6, l + 12)C(2, m + 12),$$

$$b_3 = C(7, l)C(3, m) - C(3, l)C(7, m),$$

$$c_3 = C(3, l)C(4, m) - C(4, l)C(3, m),$$

$$d_3 = C(8, l + 6)C(3, m + 6) - C(3, l + 6)C(8, m + 6),$$

$$e_3 = C(3, l + 6)C(5, m + 6) - C(5, l + 6)C(3, m + 6),$$

$$f_3 = C(9, 1 + 12)C(3, m + 12) - C(3, l + 12)C(9, m + 12),$$

$$g_3 = C(3, l + 12)C(6, m + 12) - C(6, l + 12)C(3, m + 12).$$

In the following, we omit the discussion for the case that $l = 5, m = 6$ or $l = 6, m = 5$, which is essentially the same as the other cases.

3.1.2. General fictitious scheme

Consider the geometry illustrated in Fig. 2, two sets of fictitious values $\mathbf{f}(i, j, k) := (f_1^c(i, j, k), f_2^c(i, j, k), f_3^c(i, j, k))^T$ and $\mathbf{f}(i, j + 1, k) := (f_1^c(i, j + 1, k), f_2^c(i, j + 1, k), f_3^c(i, j + 1, k))^T$ are to be determined on the irregular grid points (i, j, k) and $(i, j + 1, k)$ for discretizing central derivatives.

We denote the left domain as Ω^+ and the right one as Ω^- , in this case, $\mathbf{u}^+, \mathbf{u}^-, \mathbf{u}_y^+$, and \mathbf{u}_y^- at (x_0, y_0, z_0) can be easily approximated through interpolations and standard finite difference (FD) schemes from information in Ω^+ and Ω^- , respectively:

$$\mathbf{u}^+ = (\omega_{0, j-1}, \omega_{0, j}, \omega_{0, j+1}) \cdot (\mathbf{u}(i, j - 1, k), \mathbf{u}(i, j, k), \mathbf{f}(i, j + 1, k))^T, \tag{40}$$

$$\mathbf{u}^- = (\tilde{\omega}_{0, j}, \tilde{\omega}_{0, j+1}, \tilde{\omega}_{0, j+2}) \cdot (\mathbf{f}(i, j, k), \mathbf{u}(i, j + 1, k), \mathbf{u}(i, j + 2, k))^T, \tag{41}$$

$$\mathbf{u}_y^+ = (\omega_{1, j-1}, \omega_{1, j}, \omega_{1, j+1}) \cdot (\mathbf{u}(i, j - 1, k), \mathbf{u}(i, j, k), \mathbf{f}(i, j + 1, k))^T, \tag{42}$$

$$\mathbf{u}_y^- = (\tilde{\omega}_{1, j}, \tilde{\omega}_{1, j+1}, \tilde{\omega}_{1, j+2}) \cdot (\mathbf{f}(i, j, k), \mathbf{u}(i, j + 1, k), \mathbf{u}(i, j + 2, k))^T, \tag{43}$$

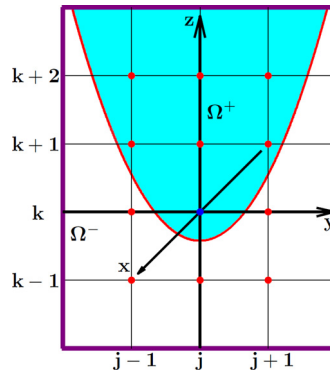


Fig. 3. An illustration of the disassociation type of irregular grid points at cross section ($x = x_i$). Fictitious values $\mathbf{f}(i, j, k)$ cannot be computed from y -direction by the aforementioned scheme. Nevertheless, they can be computed from the z -direction. In the discretization schemes, the fictitious value at (i, j, k) found from the vertical direction is utilized for both vertical and horizontal discretizations of the derivatives in the governing equation.

where $\omega_{m,n}, \tilde{\omega}_{m,n}$ denote the interpolation or finite difference weights, the first subscript n represents either the interpolation ($n = 0$) or the first order derivatives ($n = 1$) at interface point (x_0, y_0, z_0) , while the second subscript denotes the node index. All the coefficients/weights are generated from standard Lagrange polynomials [8].

We only need to compute two of the remaining four vector valued interface quantities. If \mathbf{u}_x^- and \mathbf{u}_z^- can be conveniently computed, then \mathbf{u}_x^+ and \mathbf{u}_z^+ are eliminated by using the above elimination process with setting $l = 1$ and $m = 5$.

Here we provide a detailed scheme to approximate $\frac{\partial u_1^-}{\partial z}$. Other derivatives can be approximated in the same manner. Without the loss of generality, we only demonstrate how to approximate the first component $\frac{\partial u_1^-}{\partial z}$.

As shown in Fig. 2, to approximate $\frac{\partial u_1^-}{\partial z}$, we need u_1 values along the auxiliary line $y = y_0$ on the yz -plane. However, these values are unavailable on the grid and have to be approximated by the interpolation schemes along the y -direction. Therefore six more auxiliary grid points are involved. In this situation, $\frac{\partial u_1^-}{\partial z}|_{(x_0, y_0, z_0)}$ can be approximated as

$$\frac{\partial u_1^-}{\partial z} = \begin{pmatrix} \omega_{1,k} \\ \omega_{1,k+1} \\ \omega_{1,k+2} \end{pmatrix}^T \cdot \begin{pmatrix} \omega_{0,j} & \omega_{0,j+1} & \omega_{0,j+2} & 0 & 0 & 0 & 0 & 0 & 0 \\ 0 & 0 & 0 & \omega'_{0,j} & \omega'_{0,j+1} & \omega'_{0,j+2} & 0 & 0 & 0 \\ 0 & 0 & 0 & 0 & 0 & 0 & \omega^*_{0,j} & \omega^*_{0,j+1} & \omega^*_{0,j+2} \end{pmatrix} \cdot \mathbf{U}. \quad (44)$$

Here $\mathbf{U} = (f_1^c(i, j, k), u_1(i, j + 1, k), u_1(i, j + 2, k), u_1(i, j, k + 1), u_1(i, j + 1, k + 1), u_1(i, j + 2, k + 1), u_1(i, j, k + 2), u_1(i, j + 1, k + 2), u_1(i, j + 2, k + 2))^T$. By solving the above six interface conditions (34)–(39) together, six fictitious values $\mathbf{f}(i, j, k)$ and $\mathbf{f}(i, j + 1, k)$ can be easily represented in terms of 48 function values and 12 interface jump conditions around them.

3.1.3. Matrix optimization

The MIB matrix is banded due to the reason that the interfaces are 2D surfaces and typically there is only one fictitious value on each side of the interface in a second order MIB scheme. However, to determine each pair of fictitious values, 12 auxiliary grid points are involved and their distribution affects the convergence property of the resulting MIB matrix. In most cases, the choice of these 12 auxiliary grid points is not unique. In general, it is very important to make the MIB matrix optimally symmetric and diagonally dominated so as to accelerate the speed of the convergence of the resulting linear algebraic solver. This aspect becomes more important in elasticity interface problems than in elliptic interface problems because the matrix size is much larger. We therefore select 12 auxiliary grid points as close to the interface as possible. This strategy has been employed in our earlier MIBPB II software package [32,33] for solving elliptical interface problems. A more detailed description can be found elsewhere [33]. In the present work, we utilize the same strategy to construct the MIB matrix for elasticity interface problems.

3.1.4. Fictitious scheme for interface with large curvatures

The key assumption in the above scheme is that there should be at least two grid points on each mesh line inside a subdomain so that fictitious values on the mesh line can be determined. However, when the curvature of the interface is very large, the above requirement cannot be guaranteed on all mesh sizes.

As shown in Fig. 3, the above scheme is not applicable for finding the fictitious values at grid point (i, j, k) along the y -direction, since there is only one point inside the interface along the y -direction, which is not enough for the interpolation. Nevertheless, there is no problem to find the fictitious values at grid point (i, j, k) along the z -direction. Hence, it is possible to replace the fictitious values to be found along y -direction with the fictitious values found along the z -direction or the x -direction, this treatment is referred as the disassociation technique [41].

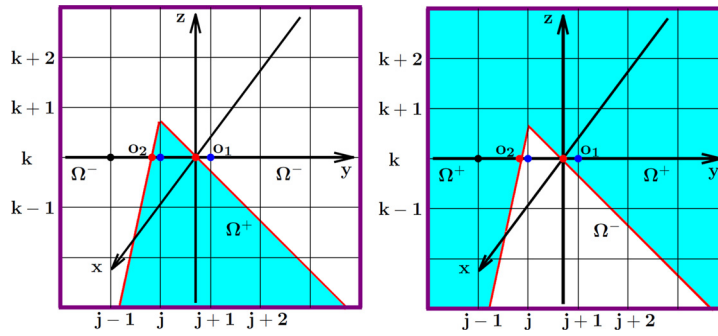


Fig. 4. Illustration of two types of sharp-edged interfaces at cross section ($x = x_i$). The jump conditions of the function values at the point o_1 and o_2 (two red points) and the jump of derivatives at o_1 are employed to compute fictitious values at two blue irregular grid points. (For interpretation of the references to color in this figure legend, the reader is referred to the web version of this article.)

Note that this replacement does not reduce the numerical accuracy in general, since if fictitious values found along z -direction have the numerical accuracy $O(h^m)$ for some integer m , this estimate holds for the fictitious values at (i, j, k) no matter how they are determined, where h is the grid size of the uniform mesh.

Remark 2. In principle, we need to make the final algebraic linear system as symmetric and banded as possible. If the fictitious values can be found along the given direction, one should avoid using the disassociation technique.

3.1.5. Fictitious scheme for interface with sharp edge

Geometric singularities, such as tips, cusps and self-intersecting surfaces, are ubiquitous in science and engineering problems. Due to the existence of geometric singularities, the schemes proposed above may not work because fictitious values cannot be determined. Therefore, it is crucial to develop some special schemes for determining fictitious values near geometric singularities.

According to the local interface geometry, the sharp-edged interface can be classified into two classes, one is locally convex, the other is locally concave, as shown in Fig. 4.

Let us discuss how to determine fictitious values at grid point (i, j, k) for the convex interface case, and the other case can be treated in the same manner.

In the MIB scheme, a pair of fictitious values is determined at one time. Suppose that the fictitious values at grid point (i, j, k) are going to be determined along the positive y -direction and the interface intersects the mesh line at point o_1 , the MIB scheme determines fictitious values at (i, j, k) and $(i, j + 1, k)$ simultaneously.

In the left chart of Fig. 4, the point $(i, j - 1, k)$ will be referred in the discretization of the interface conditions (34)–(39). Due to the sharp-edged interface, $(i, j - 1, k)$ is not in the same subdomain with (i, j, k) , and fictitious values at grid point (i, j, k) cannot be calculated directly from the interface conditions (34)–(39). In this case, one more set of fictitious values at grid point $(i, j - 1, k)$ will be involved, so that there are nine fictitious values to be determined while there are only six interface conditions available.

Note that the jump of the function values at point o_2 , which is another intersection point of the interface with the mesh line, can be utilized to compute fictitious values. Now there are nine interface conditions, namely, three jumps of function values at o_1 , three jumps of function values at o_2 and three jumps of derivatives at o_1 .

The discretization of interface conditions (34)–(39) in this sharp-edged interface situation can be obtained simply by replacing $\mathbf{u}(i, j - 1, k)$ with fictitious values $\mathbf{f}(i, j - 1, k)$, where $\mathbf{f}(i, j - 1, k) := (f_1^c(i, j - 1, k), f_2^c(i, j - 1, k), f_3^c(i, j - 1, k))^T$ is the fictitious values at node $(i, j - 1, k)$. Three more interface conditions at o_2 can be discretized as

$$[\mathbf{u}]|_{o_2} = \left(\omega'_{0,j-1}, \omega'_{0,j}, \omega'_{0,j+1} \right) \cdot \left((\mathbf{f}(i, j - 1, k), \mathbf{u}(i, j, k), \mathbf{f}(i, j + 1, k))^T - (\mathbf{u}(i, j - 1, k), \mathbf{f}(i, j, k), \mathbf{u}(i, j + 1, k))^T \right). \tag{45}$$

Fictitious values $\mathbf{f}(i, j - 1, k)$, $\mathbf{f}(i, j, k)$ and $\mathbf{f}(i, j + 1, k)$ can be calculated from the modified discretization of interface conditions (34)–(39) and Eq. (45).

3.1.6. Second order MIB finite difference for central derivatives

All the fictitious values referred in the MIB discretization of the central derivatives can be obtained by the above schemes. At any grid point the second order MIB method applies to all the central derivatives referred in the governing equations of the elasticity interface problem. At an irregular grid point if the CFD scheme refers to some grid points in the other side of the interface, the MIB scheme simply replace the function values at that point by its fictitious values. For instance, the second order MIB finite difference for $\frac{\partial^2 u_1}{\partial y^2}$ at grid point (i, j, k) and $(i, j + 1, k)$ in the left chart of Fig. 4 are given, respectively, by:

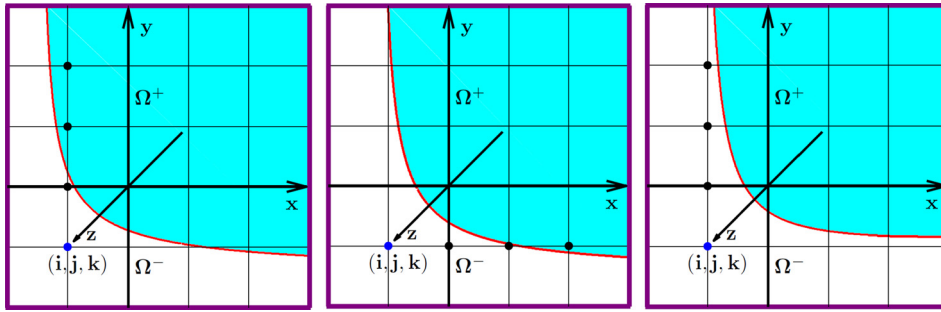


Fig. 5. Illustration of extrapolation type of irregular grid points used in cross derivatives at cross section ($z = z_k$). In the left case, fictitious value at the bottom black point and function values at other two black points are employed to approximate fictitious value at (i, j, k) . For the middle case, function values at the right most black point and fictitious values at other two black points are utilized to extrapolate fictitious value at (i, j, k) . For the right case, fictitious values at three black points are used to approximate fictitious value at (i, j, k) .

$$\frac{\partial^2 u_1}{\partial y^2}(i, j, k) = \frac{1}{h^2} (f_1^c(i, j - 1, k) - 2u_1(i, j, k) + f_1^c(i, j + 1, k)),$$

and

$$\frac{\partial^2 u_1}{\partial y^2}(i, j + 1, k) = \frac{1}{h^2} (f_1^c(i, j, k) - 2u_1(i, j + 1, k) + u_1(i, j + 2, k)).$$

3.2. General MIB algorithms for cross derivatives

The cross derivatives in the elasticity equations make the second order CFD scheme more complicated as the points referred in the CFD schemes are restricted not only to the nearest neighbor points, but also the next nearest neighbor points. This situation does not occur to the elliptic interface problems.

A critical idea of the MIB method is to reduce high-dimensional problems to locally lower-dimensional problems. As such in determining fictitious values for the elliptical interface problems, the MIB scheme carries out 1D-like extensions, which makes the MIB method highly efficient for versatile interface geometries and geometric singularities. Similar idea is applied in the present elasticity interface problem in determining fictitious values for both central derivatives and cross derivatives. Based on local interface geometric information, different schemes are designed, including, disassociation type, extrapolation type and neighbor combination type.

3.2.1. Disassociation scheme

First we define the disassociation type of fictitious values.

Definition 3.1. An irregular grid point associated with cross derivatives is called a disassociation type provided that the irregular grid point is also an irregular grid point associated with central derivatives.

The fictitious values on the disassociation type of irregular grid points for cross derivatives can be replaced by fictitious values found for the central derivatives. Their order of approximation was analyzed in an earlier paper [41].

As illustrated in Fig. 3, grid point (i, j, k) is not only irregular in central derivatives, but also irregular in cross derivatives. In this case, fictitious values for the central derivatives at grid point (i, j, k) are obtained based on the numerical scheme proposed for central derivatives.

3.2.2. Extrapolation scheme

If a grid point is irregular in the CFD scheme of the cross derivatives while regular for that of the central derivatives, the aforementioned disassociation technique fails. Further, if there exists a direction along which three values are available (function value or fictitious value), then the extrapolation method is applied. Suppose that we are seeking the fictitious values at grid point (i, j, k) and project the problem into xy -plane, according to the local geometry, the MIB scheme can be classified into three cases.

- Scheme I. Two function values and one fictitious value are used for the extrapolation. Function values at grid point $(i, j + 2, k)$ and $(i, j + 3, k)$, fictitious values at $(i, j + 1, k)$ are available and used to extrapolate fictitious values at grid point (i, j, k) , see the left chart of Fig. 5.
- Scheme II. One function value and two fictitious values are used for the extrapolation. Function values at grid point $(i + 3, j, k)$, fictitious values at $(i + 1, j, k)$ and $(i + 2, j, k)$ are available and used to extrapolate fictitious values at grid point (i, j, k) , see the middle chart of Fig. 5.

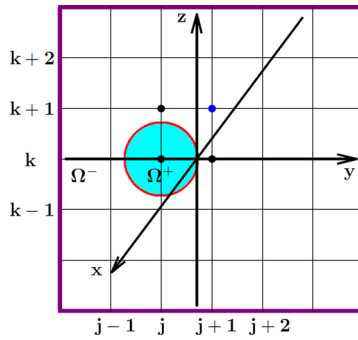


Fig. 6. Illustration of a single point situation at cross section ($x = x_i$). All the nearest and next nearest neighbor grid points are referred in the second order CFD scheme at grid point (i, j, k) . First, fictitious values at its two nearest neighbor grid point, $(i, j + 1, k)$ and $(i, j, k + 1)$ can be determined by the fictitious scheme for sharp-edged interfaces. Second, by the neighbor combination scheme, the fictitious values at the blue point $(i, j + 1, k + 1)$ can be approximated by the function or fictitious values at three black points. (For interpretation of the references to color in this figure legend, the reader is referred to the web version of this article.)

- Scheme III. Three fictitious values at grid point $(i, j + 1, k)$, $(i, j + 2, k)$ and $(i, j + 3, k)$ are applied to extrapolate the fictitious value at the grid point (i, j, k) , see the right chart of Fig. 5.

Now we consider a very special case, in which fictitious values for cross derivatives cannot be obtained with the above schemes.

As illustrated in Fig. 6, the interface is a sphere centered at (i, j, k) with radius less than grid size h . The CFD scheme at grid point (i, j, k) refers to all its distance one and two neighbor points. Note that all these points are in the other side of the interface. To attain a convergent discretization at grid point (i, j, k) , all the fictitious values at its neighbor points should be found. Here without the loss of generality, let us only consider the way to find fictitious values for u_1 at grid points $(i, j + 1, k)$, $(i, j, k + 1)$ and $(i, j + 1, k + 1)$. Due to the symmetry, other fictitious values can be obtained in the same manner.

First, the fictitious values at grid points $(i, j + 1, k)$ and $(i, j, k + 1)$ can be found by the sharp interface scheme for central derivatives. Denote the obtained fictitious values to be $f_1^c(i, j + 1, k)$ and $f_1^c(i, j, k + 1)$, respectively. Further let the analytic extension of the exact solution at these grid points to be $\hat{u}_1(i, j + 1, k)$ and $\hat{u}_1(i, j, k + 1)$. The numerical extension based on the above MIB scheme satisfies: $f_1^c(i, j + 1, k) = \hat{u}_1(i, j + 1, k) + O(h^3)$ and $f_1^c(i, j, k + 1) = \hat{u}_1(i, j, k + 1) + O(h^3)$.

Now the only fictitious value to be determined is $f_1^c(i, j + 1, k + 1)$. Based on the Taylor expansion and the above MIB extension estimates, following equations hold for the uniform Cartesian mesh with grid size h .

$$u_1(i, j + 1, k + 1) = u_1(i, j, k) + \frac{\partial u_1}{\partial y}(i, j, k)h + \frac{\partial u_1}{\partial z}(i, j, k)h + O(h^2)$$

$$u_1(i, j + 1, k) = u_1(i, j, k) + \frac{\partial u_1}{\partial y}(i, j, k)h + O(h^2)$$

$$u_1(i, j, k + 1) = u_1(i, j, k) + \frac{\partial u_1}{\partial z}(i, j, k)h + O(h^2)$$

$$f_1^c(i, j + 1, k) = \hat{u}_1(i, j + 1, k) + O(h^3),$$

$$f_1^c(i, j, k + 1) = \hat{u}_1(i, j, k + 1) + O(h^3),$$

where h is the size of the Cartesian mesh.

Therefore, let fictitious value at grid point $(i, j + 1, k + 1)$ to be:

$$f_1^c(i, j + 1, k + 1) = f_1^c(i, j + 1, k) + f_1^c(i, j, k + 1) - u_1(i, j, k).$$

By direct calculation, the following estimate holds

$$f_1^c(i, j + 1, k + 1) = \hat{u}_1(i, j + 1, k + 1) + O(h^2),$$

where $\hat{u}_1(i, j + 1, k + 1)$ is the analytic extension of the exact solution at grid point $(i, j + 1, k + 1)$.

Remark 3. The proposed scheme for finding fictitious values at $(i, j + 1, k + 1)$ may reduce the numerical accuracy, while based on numerous numerical tests, the proposed scheme is still of second order convergence globally.

3.2.3. Second order MIB finite difference for cross derivatives

It is obviously that all the fictitious values at irregular grid points are guaranteed to be found by the above extension and combination schemes. The local combination scheme may lead to some numerical accuracy reduction, however, in most

case, this scheme is used quite seldom. Based on our numerous numerical examples, the MIB scheme still has the second order numerical accuracy for both L_∞ and L_2 error for the elasticity interface problem.

Similar to the MIB discretization of the central derivatives, in the discretization of cross derivatives, when grid point from the other subdomain referred, fictitious values at that point are adopted to replace the function values in the CFD discretization. For instance, the MIB discretization of the $\frac{\partial^2 u_1}{\partial y \partial z}$ at grid point (i, j, k) in Fig. 6 is given by:

$$\frac{\partial^2 u_1}{\partial y \partial z}(i, j, k) = \frac{f_1^c(i, j + 1, k + 1) + f_1^c(i, j - 1, k - 1) - f_1^c(i, j + 1, k - 1) - f_1^c(i, j - 1, k + 1)}{4h^2}.$$

4. Numerical experiments

Numerous numerical tests are designed in this section to investigate the accuracy, efficiency and robustness of the proposed MIB method for solving 3D elasticity interface problems with both smooth and non-smooth material interfaces. We consider a large number of complex geometric shapes, including sphere, hemisphere, ellipsoid, cylinder, torus, acorn-like, apple-shaped, flower-like, and pentagon-star shapes in our tests. To examine the applicability of the proposed new MIB scheme for realistic problems, we also consider arbitrarily complex biomolecular interfaces. Both piecewise constant material parameters and position-dependent material parameters are tested in our investigation. Furthermore, problems with small and large contrast in Poisson’s ratio and shear modulus across the interface are also examined.

The standard bi-conjugate gradient method is employed to solve the linear algebraic system generated by the MIB discretization of the governing equation of the elasticity interface problems. Numerical solutions are compared to the designed analytical solution. Both L_2 and L_∞ error measurements are employed in examining the accuracy and convergence of the MIB algorithm for 3D elasticity interface problems

$$L_\infty(u_k) := \max |u_k(m, n, l) - \hat{u}_k(m, n, l)|, \quad k = 1, 2, 3; \quad \forall m = 1, 2, \dots, n_x; \quad \forall n = 1, 2, \dots, n_y; \quad \forall l = 1, 2, \dots, n_z$$

and

$$L_2 := \sqrt{\frac{1}{n_x * n_y * n_z} \sum_{m=1}^{n_x} \sum_{n=1}^{n_y} \sum_{l=1}^{n_z} (u_k(m, n, l) - \hat{u}_k(m, n, l))^2},$$

where u_k, \hat{u}_k are the numerical and exact solutions, respectively. Here L_∞ is the maximum error over all the grid points in the computational domain.

4.1. Smooth interface

4.1.1. Piecewise constant shear modulus

In this section, the proposed MIB method is tested for the piecewise constant material parameters associated with smooth material interfaces. Problems with both large and small contrasts of Poisson’s ratio and shear modulus across the interface are considered in our investigation.

Example 1. In this example, the computational domain is set to $[-3, 3] \times [-3, 3] \times [-3, 3]$ and the interface is a sphere which is defined by $x^2 + y^2 + z^2 = 4$. A sphere is the simplest irregular or complex interface in 3D. The exact solution is designed to be

$$u_1(x, y, z) = \begin{cases} x^2 + y^2 + z^2 - 4 + \cos(x) \cos(y) \cos(z), & \text{in } \Omega^+, \\ \cos(x) \cos(y) \cos(z), & \text{in } \Omega^-, \end{cases}$$

$$u_2(x, y, z) = \begin{cases} x^2 + y^2 + z^2 - 4 + xy + \cos(x) \cos(y) \cos(z), & \text{in } \Omega^+, \\ xy + \cos(x) \cos(y) \cos(z), & \text{in } \Omega^-, \end{cases}$$

and

$$u_3(x, y, z) = \begin{cases} x^2 + y^2 + z^2 - 4 + yz + \cos(x) \cos(y) \cos(z), & \text{in } \Omega^+, \\ yz + \cos(x) \cos(y) \cos(z), & \text{in } \Omega^-. \end{cases}$$

Note that the above solution guarantees the continuity of the solution across the interface. The Dirichlet boundary conditions and interface jump conditions can be derived from the above exact solution. We consider a series of three cases to test the robustness of the proposed MIB method for large contrasts in material parameters across the interface.

Case 1. First, let the piecewise constant type of Poisson’s ratio and shear modulus to be

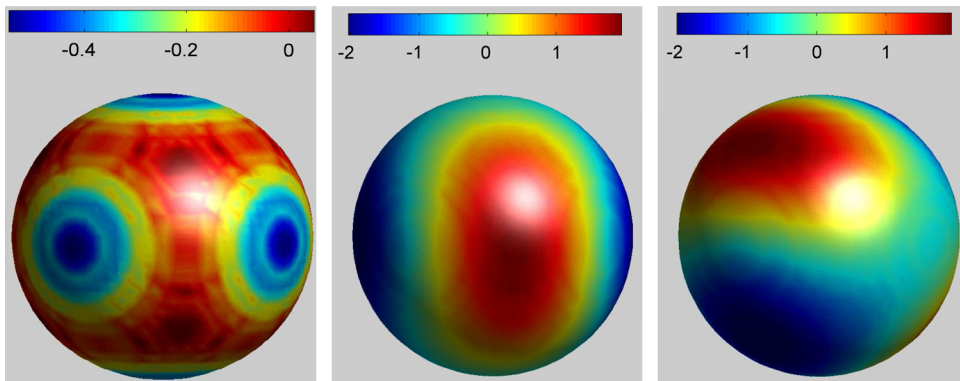
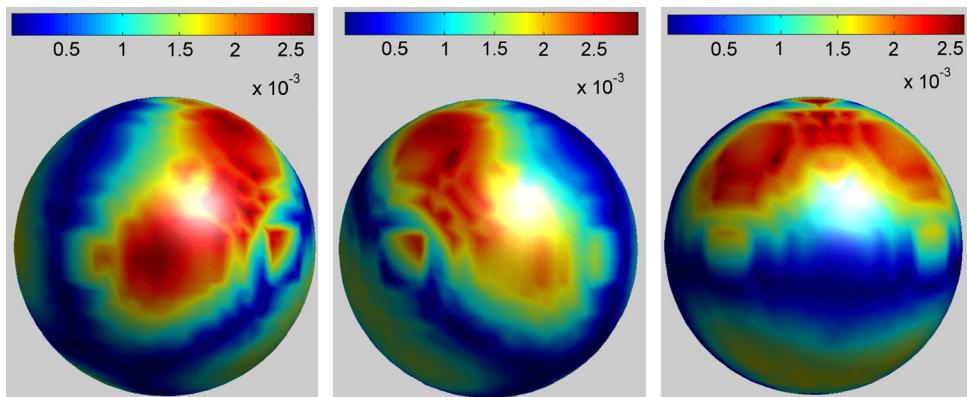
$$v = \begin{cases} v^+ = 0.20, & \text{in } \Omega^+, \\ v^- = 0.24, & \text{in } \Omega^-, \end{cases}$$

Table 1The L_∞ errors for Case 1 of Example 1.

$n_x \times n_y \times n_z$	$L_\infty(u_1)$	Order	$L_\infty(u_2)$	Order	$L_\infty(u_3)$	Order
$10 \times 10 \times 10$	6.70×10^{-2}		6.31×10^{-2}		5.68×10^{-2}	
$20 \times 20 \times 20$	1.39×10^{-2}	2.27	1.36×10^{-2}	2.21	1.31×10^{-2}	2.12
$40 \times 40 \times 40$	2.72×10^{-3}	2.35	2.94×10^{-3}	2.21	2.69×10^{-3}	2.28
$80 \times 80 \times 80$	7.58×10^{-4}	1.84	7.28×10^{-4}	2.01	7.17×10^{-4}	1.91

Table 2The L_2 errors for Case 1 of Example 1.

$n_x \times n_y \times n_z$	$L_2(u_1)$	Order	$L_2(u_2)$	Order	$L_2(u_3)$	Order
$10 \times 10 \times 10$	1.30×10^{-2}		1.29×10^{-2}		1.30×10^{-2}	
$20 \times 20 \times 20$	3.20×10^{-3}	2.02	3.20×10^{-3}	2.01	3.15×10^{-3}	2.05
$40 \times 40 \times 40$	8.34×10^{-4}	1.94	8.39×10^{-4}	1.93	8.27×10^{-4}	1.93
$80 \times 80 \times 80$	2.25×10^{-4}	1.89	2.25×10^{-4}	1.90	2.23×10^{-4}	1.89

**Fig. 7.** Numerical solution to the sphere interface problem of Case 1 with 40 grid points along each direction. Left chart: u_1 ; Middle chart: u_2 ; Right chart: u_3 .**Fig. 8.** Numerical error in solving the sphere interface problem of Case 1 with 40 grid points along each direction. Left chart: u_1 ; Middle chart: u_2 ; Right chart: u_3 .

and

$$\mu = \begin{cases} \mu^+ = 1\,500\,000, & \text{in } \Omega^+, \\ \mu^- = 2\,000\,000, & \text{in } \Omega^-. \end{cases}$$

Table 1 lists the grid refinement analysis for the L_∞ error of Case 1 of Example 1. We obtain a quite robust second order accuracy in the L_∞ error norm. It is also interesting to examine the convergence in the L_2 error norm as well. Table 2 presents the grid refinement analysis for the L_2 error of Case 1 of Example 1. We again found highly accurate solutions.

Figs. 7 and 8 illustrate the solution and error with 40 grid points along each direction. Apparently, the errors are quite small.

Table 3

The L_∞ errors for Case 2 of Example 1.

$n_x \times n_y \times n_z$	$L_\infty(u_1)$	Order	$L_\infty(u_2)$	Order	$L_\infty(u_3)$	Order
$10 \times 10 \times 10$	6.21×10^{-2}		5.95×10^{-2}		5.45×10^{-2}	
$20 \times 20 \times 20$	1.55×10^{-2}	2.00	1.55×10^{-2}	1.94	1.53×10^{-2}	1.83
$40 \times 40 \times 40$	3.13×10^{-3}	2.31	3.45×10^{-3}	2.17	3.28×10^{-3}	2.22
$80 \times 80 \times 80$	8.19×10^{-4}	1.93	7.89×10^{-4}	2.13	7.88×10^{-4}	2.06

Table 4

The L_2 errors for Case 2 of Example 1.

$n_x \times n_y \times n_z$	$L_2(u_1)$	Order	$L_2(u_2)$	Order	$L_2(u_3)$	Order
$10 \times 10 \times 10$	1.29×10^{-2}		1.28×10^{-2}		1.28×10^{-2}	
$20 \times 20 \times 20$	3.29×10^{-3}	1.97	3.28×10^{-3}	1.96	3.22×10^{-3}	1.99
$40 \times 40 \times 40$	8.49×10^{-4}	1.95	8.53×10^{-4}	1.94	8.41×10^{-4}	1.94
$80 \times 80 \times 80$	2.29×10^{-4}	1.89	2.29×10^{-4}	1.90	2.28×10^{-4}	1.89

Table 5

The L_∞ errors for Case 3 of Example 1.

$n_x \times n_y \times n_z$	$L_\infty(u_1)$	Order	$L_\infty(u_2)$	Order	$L_\infty(u_3)$	Order
$10 \times 10 \times 10$	6.70×10^{-2}		6.31×10^{-2}		5.68×10^{-2}	
$20 \times 20 \times 20$	1.40×10^{-2}	2.26	1.41×10^{-2}	1.94	1.31×10^{-2}	2.12
$40 \times 40 \times 40$	2.72×10^{-3}	2.36	2.39×10^{-3}	2.16	2.69×10^{-3}	2.28
$80 \times 80 \times 80$	7.58×10^{-4}	1.85	7.28×10^{-4}	1.72	7.17×10^{-4}	1.91

Table 6

The L_2 errors for Case 3 of Example 1.

$n_x \times n_y \times n_z$	$L_2(u_1)$	Order	$L_2(u_2)$	Order	$L_2(u_3)$	Order
$10 \times 10 \times 10$	1.30×10^{-2}		1.29×10^{-2}		1.30×10^{-2}	
$20 \times 20 \times 20$	3.19×10^{-3}	2.03	3.20×10^{-3}	2.01	3.15×10^{-3}	2.05
$40 \times 40 \times 40$	8.34×10^{-4}	1.94	8.39×10^{-4}	1.94	8.27×10^{-4}	1.93
$80 \times 80 \times 80$	2.25×10^{-4}	1.89	2.24×10^{-4}	1.91	2.23×10^{-4}	1.89

Case 2. In this case, we test the proposed MIB method for large contrasts in material parameters across the interface. We make the Poisson’s ratio to be 1000 times in contrast

$$v = \begin{cases} v^+ = 0.00024, & \text{in } \Omega^+, \\ v^- = 0.24, & \text{in } \Omega^-, \end{cases}$$

while the shear modulus remains unchanged,

$$\mu = \begin{cases} \mu^+ = 1\,500\,000, & \text{in } \Omega^+, \\ \mu^- = 2\,000\,000, & \text{in } \Omega^-. \end{cases}$$

Table 3 lists the grid refinement analysis for the L_∞ error. Similarly, Table 4 gives the grid refinement analysis for the L_2 error of Case 2. It is seen that both the accuracy and convergence are not affected by the large contrast in the Poisson’s ratio across the interface.

Case 3. Having tested the proposed MIB method for large contrast in the Poisson’s ratio, let us enlarge the contrast of the shear modulus across the interface, while the Poisson’s ratio is unchanged,

$$v = \begin{cases} v^+ = 0.20, & \text{in } \Omega^+, \\ v^- = 0.24, & \text{in } \Omega^-, \end{cases}$$

and

$$\mu = \begin{cases} \mu^+ = 2000, & \text{in } \Omega^+, \\ \mu^- = 2\,000\,000, & \text{in } \Omega^-. \end{cases}$$

Table 5 gives the grid refinement analysis for the L_∞ error of Case 3. In Table 6, we provide the grid refinement analysis for the L_2 error of Case 3.

Case 4. To further test the MIB method for the Poisson’s ratio, we will test the case with large contrast between both Poisson’s ratio and shear modulus across the interfaces, specifically, we set the Poisson’s ratio and shear modulus to:

Table 7The L_∞ errors for Case 4 of Example 1.

$n_x \times n_y \times n_z$	$L_\infty(u_1)$	Order	$L_\infty(u_2)$	Order	$L_\infty(u_3)$	Order
$10 \times 10 \times 10$	6.49×10^{-2}		6.43×10^{-2}		6.47×10^{-2}	
$20 \times 20 \times 20$	9.42×10^{-3}	2.78	9.99×10^{-3}	2.69	1.01×10^{-2}	2.68
$40 \times 40 \times 40$	2.33×10^{-3}	2.02	2.24×10^{-3}	2.16	2.14×10^{-3}	2.24
$80 \times 80 \times 80$	4.85×10^{-4}	2.26	4.62×10^{-4}	2.28	4.62×10^{-4}	2.21

Table 8The L_2 errors for Case 4 of Example 1.

$n_x \times n_y \times n_z$	$L_2(u_1)$	Order	$L_2(u_2)$	Order	$L_2(u_3)$	Order
$10 \times 10 \times 10$	1.54×10^{-2}		1.46×10^{-2}		1.47×10^{-2}	
$20 \times 20 \times 20$	2.46×10^{-3}	2.65	2.45×10^{-3}	2.58	2.47×10^{-3}	2.57
$40 \times 40 \times 40$	6.73×10^{-4}	1.87	6.57×10^{-4}	1.90	6.54×10^{-4}	1.92
$80 \times 80 \times 80$	1.60×10^{-4}	2.07	1.59×10^{-4}	2.05	1.59×10^{-4}	2.04

Table 9The L_∞ errors for Case 1 of Example 2.

$n_x \times n_y \times n_z$	$L_\infty(u_1)$	Order	$L_\infty(u_2)$	Order	$L_\infty(u_3)$	Order
$10 \times 10 \times 10$	6.38×10^{-2}		5.93×10^{-2}		6.17×10^{-2}	
$20 \times 20 \times 20$	1.35×10^{-2}	2.24	1.33×10^{-2}	2.16	1.35×10^{-2}	2.19
$40 \times 40 \times 40$	2.67×10^{-3}	2.34	2.97×10^{-3}	2.16	2.70×10^{-3}	2.32
$80 \times 80 \times 80$	6.28×10^{-4}	2.09	6.52×10^{-4}	2.19	5.91×10^{-4}	2.19

Table 10The L_2 errors for Case 1 of Example 2.

$n_x \times n_y \times n_z$	$L_2(u_1)$	Order	$L_2(u_2)$	Order	$L_2(u_3)$	Order
$10 \times 10 \times 10$	1.33×10^{-2}		1.32×10^{-2}		1.57×10^{-2}	
$20 \times 20 \times 20$	3.35×10^{-3}	1.99	3.33×10^{-3}	1.99	3.44×10^{-3}	2.19
$40 \times 40 \times 40$	8.61×10^{-4}	1.96	8.61×10^{-4}	1.95	8.65×10^{-4}	1.99
$80 \times 80 \times 80$	2.01×10^{-4}	2.10	2.02×10^{-4}	2.09	2.01×10^{-4}	2.11

$$\nu = \begin{cases} \nu^+ = 0.20, & \text{in } \Omega^+, \\ \nu^- = 0.00024, & \text{in } \Omega^-, \end{cases}$$

and

$$\mu = \begin{cases} \mu^+ = 2000, & \text{in } \Omega^+, \\ \mu^- = 2\,000\,000, & \text{in } \Omega^-. \end{cases}$$

Table 7 gives the grid refinement analysis for the L_∞ error of Case 4. In Table 8, we provide the grid refinement analysis for the L_2 error of Case 4.

Obviously, the proposed method is of second order convergence in both L_∞ and L_2 error norms in all four cases in Example 1.

Example 2. In this example, we modify the interface geometry. Let the computational domain be $[-3, 3] \times [-3, 3] \times [-3, 3]$ and the interface be given as a hemisphere

$$\begin{cases} x^2 + y^2 + z^2 = 4, \\ z \geq 0. \end{cases}$$

To ensure the continuity of the solution across the interface, the analytic solution adopted in this example is the same as that in Example 1. In this example, we also test the numerical scheme for three different cases of Poisson's ratio and shear modulus, in each case the material parameters are inherited from the corresponded case in Example 1.

Case 1. Table 9 gives the grid refinement analysis of the L_∞ error. Similarly the grid refinement analysis of the L_2 error is presented in Table 10. It is seen that both the level of accuracy and the order of convergence are the same as those in the Case 1 of Example 1, which suggests that the proposed method is sensitive to the change in the geometry.

Figs. 9 and 10 show the numerical solution and error for Case 1 of Example 2, respectively. The number of grids is 40 along each direction of the computational domain.

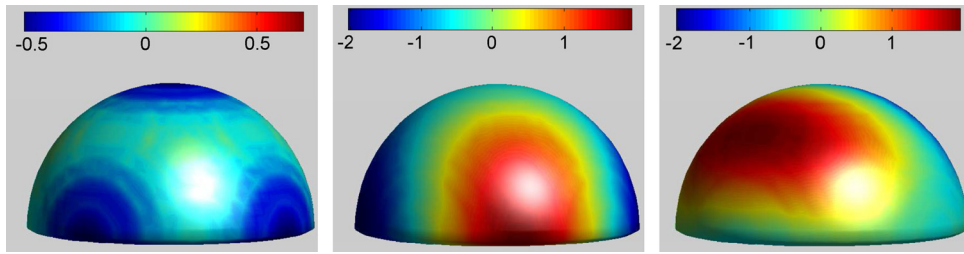


Fig. 9. Numerical solution for Case 1 of the hemisphere interface problem with 40 grid points along each direction of the computational domain. Left chart: u_1 ; Middle chart: u_2 ; Right chart: u_3 .

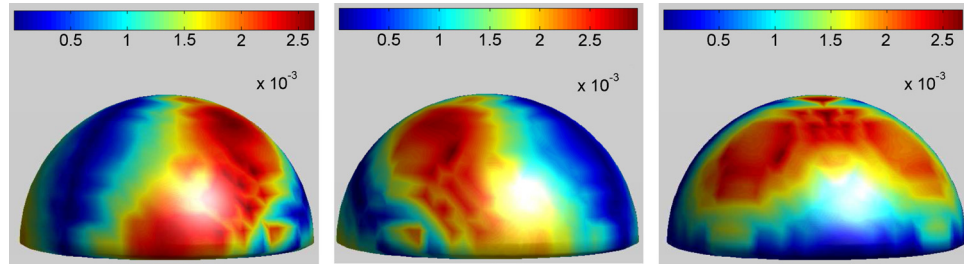


Fig. 10. Numerical error for Case 1 of the hemisphere interface problem with 40 grids along each direction of the computational domain. Left chart: u_1 ; Middle chart: u_2 ; Right chart: u_3 .

Table 11

The L_∞ errors for Case 2 of Example 2.

$n_x \times n_y \times n_z$	$L_\infty(u_1)$	Order	$L_\infty(u_2)$	Order	$L_\infty(u_3)$	Order
$10 \times 10 \times 10$	5.87×10^{-2}		5.59×10^{-2}		5.93×10^{-2}	
$20 \times 20 \times 20$	1.48×10^{-2}	1.99	1.50×10^{-2}	1.90	1.58×10^{-2}	1.91
$40 \times 40 \times 40$	3.00×10^{-3}	2.30	3.47×10^{-3}	2.11	3.30×10^{-3}	2.26
$80 \times 80 \times 80$	6.80×10^{-4}	2.14	7.00×10^{-4}	2.31	6.72×10^{-4}	2.30

Table 12

The L_2 errors for Case 2 of Example 2.

$n_x \times n_y \times n_z$	$L_2(u_1)$	Order	$L_2(u_2)$	Order	$L_2(u_3)$	Order
$10 \times 10 \times 10$	1.33×10^{-2}		1.32×10^{-2}		1.62×10^{-2}	
$20 \times 20 \times 20$	3.42×10^{-3}	1.96	3.40×10^{-3}	1.96	3.55×10^{-3}	2.19
$40 \times 40 \times 40$	8.73×10^{-4}	1.97	8.75×10^{-4}	1.96	8.89×10^{-4}	2.00
$80 \times 80 \times 80$	2.02×10^{-4}	2.11	2.02×10^{-4}	2.11	2.13×10^{-4}	2.06

Table 13

The L_∞ errors for Case 3 of Example 2.

$n_x \times n_y \times n_z$	$L_\infty(u_1)$	Order	$L_\infty(u_2)$	Order	$L_\infty(u_3)$	Order
$10 \times 10 \times 10$	6.38×10^{-2}		5.93×10^{-2}		6.17×10^{-2}	
$20 \times 20 \times 20$	1.35×10^{-2}	2.24	1.33×10^{-2}	2.16	1.35×10^{-2}	2.19
$40 \times 40 \times 40$	2.67×10^{-3}	2.34	2.97×10^{-3}	2.16	2.70×10^{-3}	2.32
$80 \times 80 \times 80$	6.28×10^{-4}	2.09	6.52×10^{-4}	2.19	5.91×10^{-4}	2.19

Case 2. Table 11 gives the grid refinement analysis of the L_∞ error for the large contrast between Poisson’s ratio across the interface. The numerical behavior is quite similar to that in Case 2 of Example 1.

Table 12 lists the grid refinement analysis of the L_2 error for the large contrast between Poisson’s ratio across the interface. We observe the second order convergence in the L_2 error norm.

Case 3. Table 13 offers the grid refinement analysis of the L_∞ error for the large contrast between shear modulus across the interface. Table 14 gives the grid refinement analysis of the L_2 error.

Case 4. Table 15 offers the grid refinement analysis of the L_∞ error for the large contrast between both Poisson ratio and shear modulus across the interface. Table 16 gives the grid refinement analysis of the L_2 error.

Table 14The L_2 errors for Case 3 of Example 2.

$n_x \times n_y \times n_z$	$L_2(u_1)$	Order	$L_2(u_2)$	Order	$L_2(u_3)$	Order
$10 \times 10 \times 10$	1.33×10^{-2}		1.32×10^{-2}		1.57×10^{-2}	
$20 \times 20 \times 20$	3.35×10^{-3}	1.99	3.33×10^{-3}	1.99	3.44×10^{-3}	2.19
$40 \times 40 \times 40$	8.60×10^{-4}	1.96	8.61×10^{-4}	1.95	8.65×10^{-4}	1.99
$80 \times 80 \times 80$	2.01×10^{-4}	2.10	2.00×10^{-4}	2.10	2.00×10^{-4}	2.11

Table 15The L_∞ errors for Case 4 of Example 2.

$n_x \times n_y \times n_z$	$L_\infty(u_1)$	Order	$L_\infty(u_2)$	Order	$L_\infty(u_3)$	Order
$10 \times 10 \times 10$	5.68×10^{-2}		5.32×10^{-2}		5.17×10^{-2}	
$20 \times 20 \times 20$	7.61×10^{-3}	2.90	7.87×10^{-3}	2.76	8.03×10^{-3}	2.69
$40 \times 40 \times 40$	1.89×10^{-3}	2.01	1.91×10^{-3}	2.04	2.26×10^{-3}	1.83
$80 \times 80 \times 80$	5.42×10^{-4}	1.80	5.53×10^{-4}	1.79	5.03×10^{-4}	2.17

Table 16The L_2 errors for Case 4 of Example 2.

$n_x \times n_y \times n_z$	$L_2(u_1)$	Order	$L_2(u_2)$	Order	$L_2(u_3)$	Order
$10 \times 10 \times 10$	9.65×10^{-3}		9.67×10^{-3}		9.82×10^{-3}	
$20 \times 20 \times 20$	2.22×10^{-3}	2.12	2.22×10^{-3}	2.12	2.24×10^{-3}	2.13
$40 \times 40 \times 40$	5.89×10^{-4}	1.91	5.89×10^{-4}	1.91	6.04×10^{-4}	1.89
$80 \times 80 \times 80$	1.16×10^{-4}	2.34	1.51×10^{-4}	1.96	1.38×10^{-4}	2.13

Table 17The L_∞ errors for Case 1 of Example 3.

$n_x \times n_y \times n_z$	$L_\infty(u_1)$	Order	$L_\infty(u_2)$	Order	$L_\infty(u_3)$	Order
$10 \times 10 \times 10$	3.96×10^{-2}		5.23×10^{-2}		3.16×10^{-2}	
$20 \times 20 \times 20$	1.52×10^{-2}	1.38	1.31×10^{-2}	2.00	8.07×10^{-2}	1.97
$40 \times 40 \times 40$	2.82×10^{-3}	2.43	3.45×10^{-3}	1.93	1.90×10^{-3}	2.09
$80 \times 80 \times 80$	6.99×10^{-4}	2.01	8.81×10^{-4}	1.97	4.83×10^{-4}	1.98

In all these four cases in Example 2, the second order convergence in both L_∞ and L_2 errors is essentially reached. The level of accuracy is the same as that found in Example 1.

Example 3. In this example, the computational domain is set to be: $[-3, 3] \times [-4, 4] \times [-2, 2]$ with an ellipsoid interface defined as $\frac{x^2}{4} + \frac{y^2}{9} + z^2 = 1$.

The Dirichlet boundary condition and interface jump conditions are determined from the following exact solution

$$u_1(x, y, z) = \begin{cases} \frac{x^2}{4} + \frac{y^2}{9} + z^2 - 1 + \cos(x) \cos(y) \cos(z), & \text{in } \Omega^+, \\ \cos(x) \cos(y) \cos(z), & \text{in } \Omega^-, \end{cases}$$

$$u_2(x, y, z) = \begin{cases} \frac{x^2}{4} + \frac{y^2}{9} + z^2 - 1 + xy + \cos(x) \cos(y) \cos(z), & \text{in } \Omega^+, \\ xy + \cos(x) \cos(y) \cos(z), & \text{in } \Omega^-, \end{cases}$$

and

$$u_3(x, y, z) = \begin{cases} \frac{x^2}{4} + \frac{y^2}{9} + z^2 - 1 + yz + \cos(x) \cos(y) \cos(z), & \text{in } \Omega^+, \\ yz + \cos(x) \cos(y) \cos(z), & \text{in } \Omega^-. \end{cases}$$

Obviously, the property of solution continuity across the interface is also satisfied in the above solution. In this example, three different cases of the material parameters used in the above two examples are adopted to examine the sensitivity of the proposed MIB method to the change in interface geometry.

Case 1. Grid refinement analysis for L_∞ error is demonstrated in Table 17 for the ellipsoid interface. A similar analysis for L_2 error is listed in Table 18 for the ellipsoid interface. Again, we see the same type of behavior in accuracy and convergence as that in last few examples.

The numerical solution and error of the ellipsoid interface problem are illustrated in Figs. 11, 12 with 40 grid points along each direction of the computational domain.

Table 18
The L_2 errors for Case 1 of Example 3.

$n_x \times n_y \times n_z$	$L_2(u_1)$	Order	$L_2(u_2)$	Order	$L_2(u_3)$	Order
$10 \times 10 \times 10$	1.16×10^{-2}		1.45×10^{-2}		6.72×10^{-2}	
$20 \times 20 \times 20$	3.54×10^{-3}	1.71	3.96×10^{-3}	1.88	1.86×10^{-3}	1.85
$40 \times 40 \times 40$	8.61×10^{-4}	2.04	1.08×10^{-4}	1.88	4.78×10^{-4}	1.96
$80 \times 80 \times 80$	2.23×10^{-4}	1.95	2.86×10^{-4}	1.92	1.26×10^{-4}	1.93

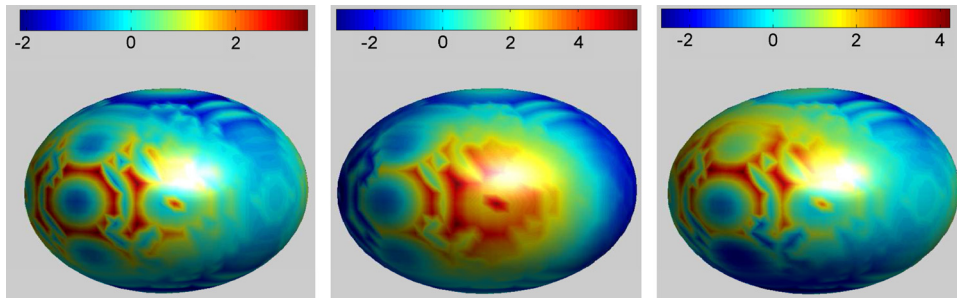


Fig. 11. Numerical solution for Case 1 of the ellipsoid interface problem with 40 grid points along each direction of the computational domain. Left chart: u_1 ; Middle chart: u_2 ; Right chart: u_3 .

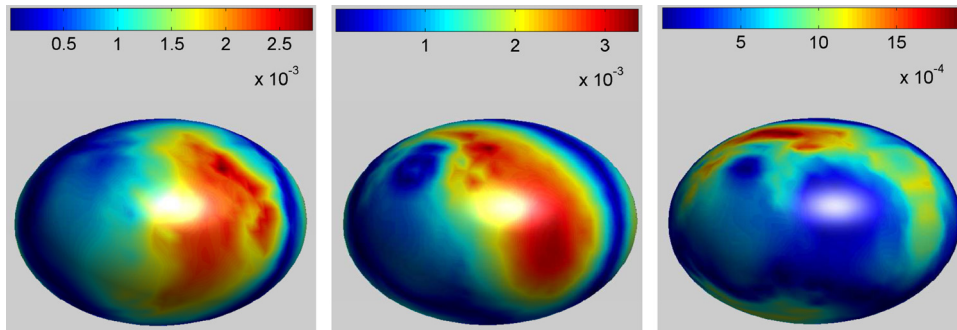


Fig. 12. Numerical error for Case 1 of the ellipsoid interface problem with 40 grid points along each direction of the computational domain. Left chart: u_1 ; Middle chart: u_2 ; Right chart: u_3 .

Table 19
The L_∞ errors for Case 2 of Example 3.

$n_x \times n_y \times n_z$	$L_\infty(u_1)$	Order	$L_\infty(u_2)$	Order	$L_\infty(u_3)$	Order
$10 \times 10 \times 10$	5.00×10^{-2}		5.10×10^{-2}		3.37×10^{-2}	
$20 \times 20 \times 20$	1.26×10^{-2}	1.99	1.37×10^{-2}	1.90	8.01×10^{-2}	2.07
$40 \times 40 \times 40$	3.24×10^{-3}	1.96	3.63×10^{-3}	1.92	2.00×10^{-3}	2.00
$80 \times 80 \times 80$	7.73×10^{-4}	2.07	9.98×10^{-4}	1.87	5.15×10^{-4}	1.96

Table 20
The L_2 errors for Case 2 of Example 3.

$n_x \times n_y \times n_z$	$L_2(u_1)$	Order	$L_2(u_2)$	Order	$L_2(u_3)$	Order
$10 \times 10 \times 10$	1.20×10^{-2}		1.50×10^{-2}		6.93×10^{-3}	
$20 \times 20 \times 20$	3.77×10^{-3}	1.67	4.13×10^{-3}	1.70	1.91×10^{-3}	1.86
$40 \times 40 \times 40$	9.18×10^{-4}	2.04	1.12×10^{-4}	1.88	4.88×10^{-4}	1.97
$80 \times 80 \times 80$	2.36×10^{-4}	1.96	2.94×10^{-4}	1.93	1.30×10^{-4}	1.91

Case 2. Grid refinement analysis for the L_∞ error is demonstrated in Table 19. A similar grid refinement analysis for L_2 error is illustrated in Table 20.

Case 3. Grid refinement analysis for L_∞ error is demonstrated in Table 21. We also illustrate the grid refinement analysis in terms of L_2 error in Table 22.

Table 21The L_∞ errors for Case 3 of Example 3.

$n_x \times n_y \times n_z$	$L_\infty(u_1)$	Order	$L_\infty(u_2)$	Order	$L_\infty(u_3)$	Order
$10 \times 10 \times 10$	3.97×10^{-2}		5.23×10^{-2}		3.16×10^{-2}	
$20 \times 20 \times 20$	1.22×10^{-2}	1.70	1.31×10^{-2}	2.00	8.07×10^{-2}	1.97
$40 \times 40 \times 40$	2.82×10^{-3}	2.11	3.45×10^{-3}	1.93	1.90×10^{-3}	2.07
$80 \times 80 \times 80$	6.99×10^{-4}	2.01	8.81×10^{-4}	1.97	4.82×10^{-4}	1.98

Table 22The L_2 errors for Case 3 of Example 3.

$n_x \times n_y \times n_z$	$L_2(u_1)$	Order	$L_2(u_2)$	Order	$L_2(u_3)$	Order
$10 \times 10 \times 10$	1.16×10^{-2}		1.45×10^{-2}		7.72×10^{-2}	
$20 \times 20 \times 20$	3.24×10^{-3}	1.84	3.96×10^{-3}	1.99	1.86×10^{-3}	2.05
$40 \times 40 \times 40$	8.61×10^{-4}	1.91	1.08×10^{-3}	1.87	4.78×10^{-4}	1.96
$80 \times 80 \times 80$	2.23×10^{-4}	1.95	2.86×10^{-4}	1.92	1.26×10^{-4}	1.92

Table 23The L_∞ errors for Case 4 of Example 3.

$n_x \times n_y \times n_z$	$L_\infty(u_1)$	Order	$L_\infty(u_2)$	Order	$L_\infty(u_3)$	Order
$10 \times 10 \times 10$	2.89×10^{-2}		3.23×10^{-2}		2.23×10^{-2}	
$20 \times 20 \times 20$	7.27×10^{-3}	1.99	8.06×10^{-3}	2.00	7.55×10^{-3}	1.57
$40 \times 40 \times 40$	1.53×10^{-3}	2.25	2.08×10^{-3}	1.95	1.55×10^{-3}	2.28
$80 \times 80 \times 80$	3.77×10^{-4}	2.02	5.32×10^{-4}	1.97	3.42×10^{-4}	2.18

Table 24The L_2 errors for Case 4 of Example 3.

$n_x \times n_y \times n_z$	$L_2(u_1)$	Order	$L_2(u_2)$	Order	$L_2(u_3)$	Order
$10 \times 10 \times 10$	7.99×10^{-3}		8.71×10^{-3}		5.42×10^{-3}	
$20 \times 20 \times 20$	2.20×10^{-3}	1.86	2.37×10^{-3}	1.88	1.64×10^{-3}	1.72
$40 \times 40 \times 40$	5.49×10^{-4}	2.00	6.63×10^{-4}	1.84	3.95×10^{-4}	2.05
$80 \times 80 \times 80$	1.42×10^{-4}	1.95	1.75×10^{-4}	1.92	9.95×10^{-5}	1.99

Case 4. In the case that with large contrast between both Poisson's ratio and shear modulus, as the same in the above two examples. Grid refinement analysis for L_∞ error is demonstrated in Table 23. We also illustrate the grid refinement analysis in terms of L_2 error in Table 24.

The second order convergence of the MIB algorithm is essentially observed from all the numerical tests in Example 3.

Remark 4. In all the above examples, the continuity of the solution across the interface, i.e., the no fracture condition, has been carefully maintained in designing the analytical solutions. However, for real world problems, having fractures at the interface is very common. In the following two numerical experiments, the continuity condition of the function values across the interface is dropped. We test our method for handling general jumps of the function values across the interface. Numerically, this situation is slightly more difficult to deal with.

Example 4. The computational domain is set to be $[-2, 2] \times [-2, 2] \times [-2, 4.4]$ with a cylinder interface defined as

$$\begin{cases} x^2 + y^2 = \frac{\pi^2}{4}, \\ z \leq \pi, \\ z \geq 0. \end{cases}$$

The Dirichlet boundary condition and interface conditions are determined from the following exact solutions.

$$u_1(x, y, z) = \begin{cases} x^2 + y^2 + z^2 - 4, & \text{in } \Omega^+, \\ \cos(x) \cos(y) \cos(z), & \text{in } \Omega^-, \end{cases}$$

$$u_2(x, y, z) = \begin{cases} x^2 + y^2 + z^2 + xy - 4, & \text{in } \Omega^+, \\ xy + \cos(x) \cos(y) \cos(z), & \text{in } \Omega^-, \end{cases}$$

and

$$u_3(x, y, z) = \begin{cases} x^2 + y^2 + z^2 + yz - 4, & \text{in } \Omega^+, \\ yz + \cos(x) \cos(y) \cos(z), & \text{in } \Omega^-. \end{cases}$$

Table 25
The L_∞ errors of Example 4.

$n_x \times n_y \times n_z$	$L_\infty(u_1)$	Order	$L_\infty(u_2)$	Order	$L_\infty(u_3)$	Order
$20 \times 20 \times 20$	4.68×10^{-3}		4.68×10^{-3}		7.07×10^{-3}	
$40 \times 40 \times 40$	1.16×10^{-3}	2.01	1.17×10^{-3}	2.00	1.74×10^{-3}	2.02
$80 \times 80 \times 80$	2.87×10^{-4}	2.02	2.91×10^{-4}	2.00	4.23×10^{-4}	2.04

Table 26
The L_2 errors of Example 4.

$n_x \times n_y \times n_z$	$L_2(u_1)$	Order	$L_2(u_2)$	Order	$L_2(u_3)$	Order
$20 \times 20 \times 20$	1.04×10^{-3}		1.04×10^{-3}		1.58×10^{-3}	
$40 \times 40 \times 40$	2.61×10^{-4}	1.99	2.62×10^{-4}	1.99	3.86×10^{-4}	2.03
$80 \times 80 \times 80$	6.69×10^{-5}	1.96	6.77×10^{-5}	1.95	9.77×10^{-5}	1.98

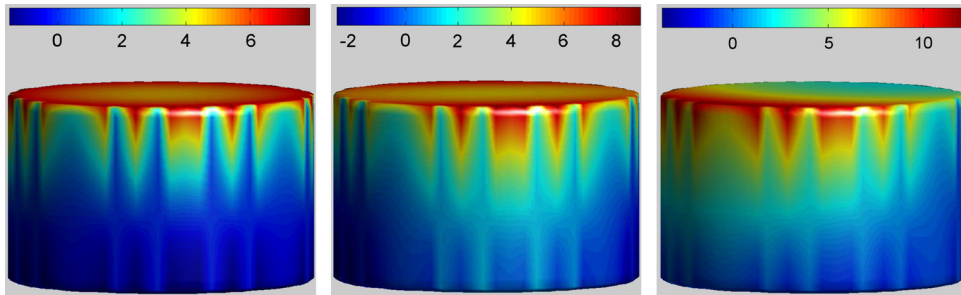


Fig. 13. Numerical solution to the cylinder interface problem with 40 grid points along each direction of the computational domain. Left chart: u_1 ; Middle chart: u_2 ; Right chart: u_3 .

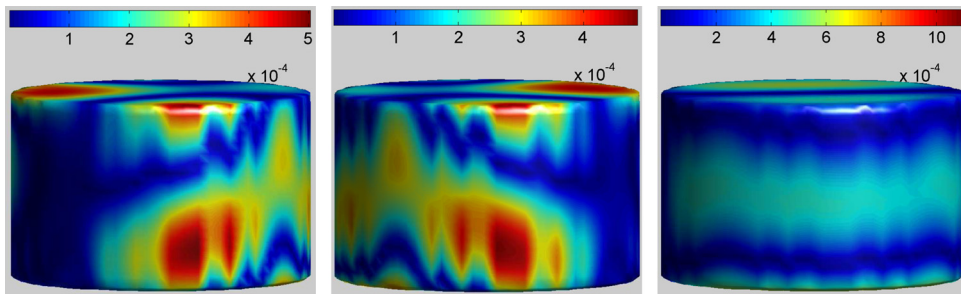


Fig. 14. Numerical error of solving the cylinder interface problem with 40 grid points along each direction of the computational domain. Left chart: u_1 ; Middle chart: u_2 ; Right chart: u_3 .

The values of the Poisson’s ratio and shear modulus are, respectively, set to

$$\nu = \begin{cases} \nu^+ = 0.20, & \text{in } \Omega^+, \\ \nu^- = 0.24, & \text{in } \Omega^- \end{cases}$$

and

$$\mu = \begin{cases} \mu^+ = 1\,500\,000, & \text{in } \Omega^+, \\ \mu^- = 2\,000\,000, & \text{in } \Omega^-. \end{cases}$$

Table 25 offers the grid refinement analysis of the L_∞ error for Example 4. Similar grid refinement analysis of the L_2 error is given in Table 26 for Example 4. A high level of accuracy and a robust order of convergence are observed from these tests.

Numerical solution and error are depicted in Figs. 13 and 14, respectively, where 40 grid points are used along each direction of the computational domain. Obviously, the error is very small in all of three solutions.

Example 5. Geometric complexity is a major issue in interface problems. It is often the case that numerical methods designed for simple interface geometries do not work for complex interface geometries. In this example, we consider a more complicated interface, which is defined to be a torus

Table 27
The L_∞ errors of Example 5.

$n_x \times n_y \times n_z$	$L_\infty(u_1)$	Order	$L_\infty(u_2)$	Order	$L_\infty(u_3)$	Order
$20 \times 20 \times 20$	2.04×10^{-1}		2.04×10^{-1}		1.12×10^{-1}	
$40 \times 40 \times 40$	4.14×10^{-2}	2.30	4.05×10^{-2}	2.33	2.34×10^{-2}	2.09
$80 \times 80 \times 80$	1.24×10^{-2}	1.74	1.09×10^{-2}	1.89	4.66×10^{-3}	1.97

Table 28
The L_2 errors of Example 5.

$n_x \times n_y \times n_z$	$L_2(u_1)$	Order	$L_2(u_2)$	Order	$L_2(u_3)$	Order
$20 \times 20 \times 20$	4.54×10^{-2}		4.52×10^{-2}		1.87×10^{-2}	
$40 \times 40 \times 40$	1.12×10^{-2}	1.71	1.10×10^{-2}	2.04	4.40×10^{-3}	2.09
$80 \times 80 \times 80$	2.92×10^{-3}	2.04	2.90×10^{-3}	1.92	1.12×10^{-3}	1.97

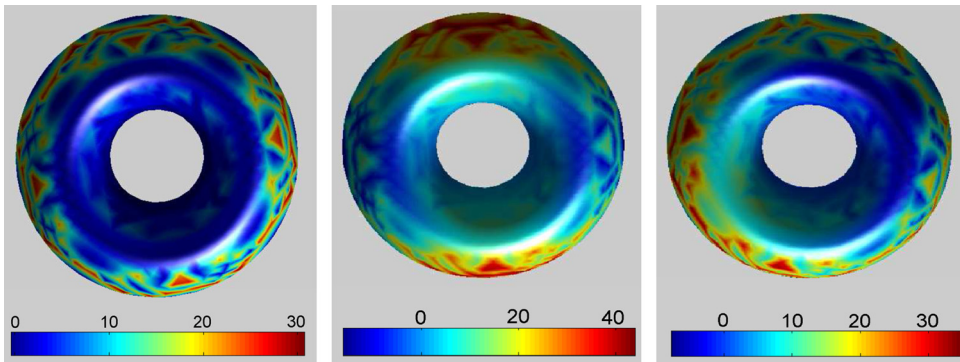


Fig. 15. Numerical solution to the torus interface problem with 40 grid points along each direction of the computational domain. Left chart: u_1 ; Middle chart: u_2 ; Right chart: u_3 .

$$\begin{cases} x(\theta, \phi) = (R + r \cos \phi) \cos \theta, \\ y(\theta, \phi) = (R + r \sin \phi) \sin \theta, \\ z(\theta, \phi) = r \sin \phi, \end{cases}$$

where $\theta, \phi \in [0, 2\pi]$ are two parameters. The computational domain is set to be $[-10, 10] \times [-10, 10] \times [-5, 5]$.

The above torus can also be represented as

$$(R - \sqrt{x^2 + y^2})^2 + z^2 = r^2.$$

We set $R = 4, r = 2$ in our numerical experiments.

The Poisson's ratio, shear modulus and designed analytic solution in Example 4 are adopted for this example. Grid refinement analysis in terms of L_∞ error is given in Table 27. A similar grid refinement analysis in terms of L_2 error is given Table 28. Although there is some small fluctuation in the convergent order, the second order convergence is essentially obtained in this test.

Figs. 15 and 16 illustrate the numerical solution and the error in a $40 \times 40 \times 40$ mesh. Note that errors appear large in this test example. However, the amplitude of the solution is much larger too, due to a much larger computational domain.

Example 6. For the last example of the smooth interface with piecewise constant material parameters, we consider a more complicated interface geometry, i.e., a flower-like cylinder interface. The interface can be represented as

$$\begin{cases} r = \frac{5}{2} + \frac{5}{7} \sin 5\theta, \\ -\frac{2}{3} \leq z \leq \frac{2}{3}, \end{cases}$$

where $r = \sqrt{x^2 + y^2}$ and $\theta = \arctan \frac{y}{x}$. The computational domain is set to $[-5, 5] \times [-5, 5] \times [-2, 2]$.

Material parameters and exact solutions designed in Example 4 are utilized in this example. Grid refinement analysis in terms of L_∞ error is given in Table 29 and a similar analysis in terms of L_2 error is given in Table 30. It is quite interesting to see that good convergent orders are attained.

Figs. 17 and 18 demonstrate the solution and error of the flower-liked interface problem with grid size 0.125. Note that the error amplitude depends on the mesh size.

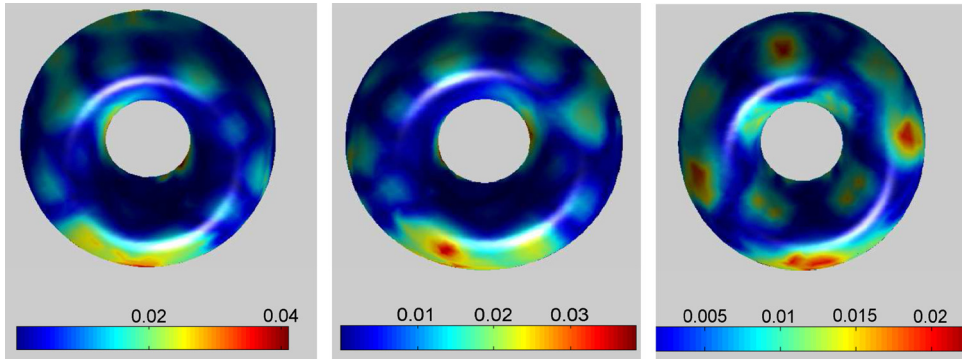


Fig. 16. Numerical error to the torus interface problem with 40 grid points along each direction of the computational domain, Left chart: u_1 ; Middle chart: u_2 ; Right chart: u_3 .

Table 29

The L_∞ errors of Example 6.

Grid size	$L_\infty(u_1)$	Order	$L_\infty(u_2)$	Order	$L_\infty(u_3)$	Order
0.5	4.29×10^{-2}		4.49×10^{-2}		1.95×10^{-2}	
0.25	9.04×10^{-3}	2.25	9.46×10^{-3}	2.25	4.97×10^{-3}	1.97
0.125	1.96×10^{-3}	2.21	2.17×10^{-3}	2.03	7.02×10^{-3}	2.82

Table 30

The L_2 errors of Example 6.

Grid size	$L_2(u_1)$	Order	Error $L_2(u_2)$	Order	$L_2(u_3)$	Order
0.5	4.12×10^{-3}		4.96×10^{-3}		2.35×10^{-3}	
0.25	9.90×10^{-4}	2.06	1.11×10^{-3}	2.16	4.10×10^{-4}	2.52
0.125	2.11×10^{-4}	2.23	2.38×10^{-4}	2.22	7.68×10^{-5}	2.42

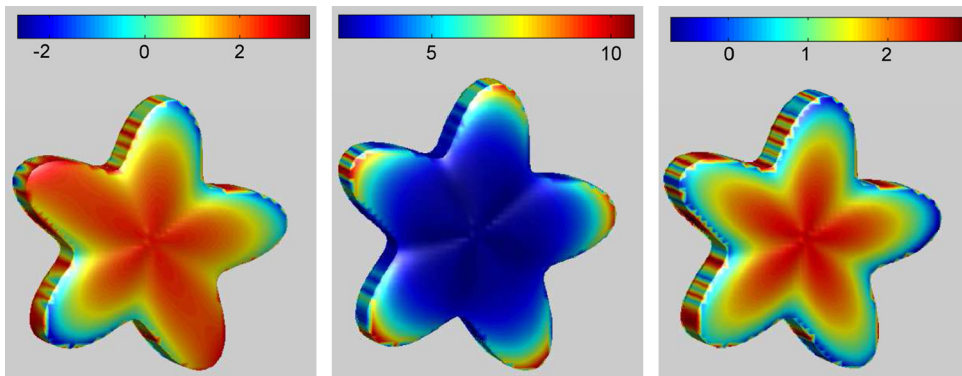


Fig. 17. Numerical solution to the flower interface problem with grid size 0.125. Left chart: u_1 ; Middle chart: u_2 ; Right chart: u_3 .

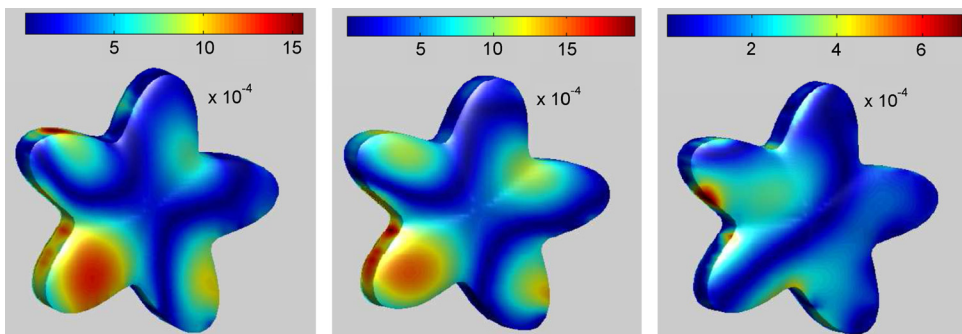


Fig. 18. Numerical error for solving the flower interface problem with grid size 0.125. Left chart: u_1 ; Middle chart: u_2 ; Right chart: u_3 .

Table 31The L_∞ errors of Example 7.

$n_x \times n_y \times n_z$	$L_\infty(u_1)$	Order	$L_\infty(u_2)$	Order	$L_\infty(u_3)$	Order
$10 \times 10 \times 10$	6.61×10^{-2}		6.27×10^{-2}		5.67×10^{-2}	
$20 \times 20 \times 20$	1.37×10^{-2}	2.27	1.34×10^{-2}	2.27	1.31×10^{-2}	2.11
$40 \times 40 \times 40$	2.66×10^{-3}	2.36	2.84×10^{-3}	2.24	2.67×10^{-3}	2.29
$80 \times 80 \times 80$	7.41×10^{-4}	1.90	7.15×10^{-4}	1.99	7.26×10^{-4}	1.89

Table 32The L_2 errors of Example 7.

$n_x \times n_y \times n_z$	$L_2(u_1)$	Order	Error $L_2(u_2)$	Order	$L_2(u_3)$	Order
$10 \times 10 \times 10$	1.28×10^{-2}		1.28×10^{-2}		1.29×10^{-2}	
$20 \times 20 \times 20$	3.18×10^{-3}	2.01	3.19×10^{-3}	2.00	3.14×10^{-3}	2.04
$40 \times 40 \times 40$	8.30×10^{-4}	1.94	8.36×10^{-4}	1.93	8.26×10^{-4}	1.93
$80 \times 80 \times 80$	2.24×10^{-4}	1.89	2.24×10^{-4}	1.90	2.23×10^{-4}	1.89

Table 33The L_∞ errors of Example 8.

$n_x \times n_y \times n_z$	$L_\infty(u_1)$	Order	$L_\infty(u_2)$	Order	$L_\infty(u_3)$	Order
$10 \times 10 \times 10$	1.85×10^{-2}		1.85×10^{-2}		3.14×10^{-2}	
$20 \times 20 \times 20$	4.68×10^{-3}	1.98	4.68×10^{-3}	1.98	7.07×10^{-3}	2.15
$40 \times 40 \times 40$	1.15×10^{-3}	2.02	1.17×10^{-3}	2.00	1.74×10^{-3}	2.02
$80 \times 80 \times 80$	2.99×10^{-4}	1.94	3.19×10^{-4}	1.87	4.23×10^{-4}	2.01

Table 34The L_2 errors of Example 8.

$n_x \times n_y \times n_z$	$L_2(u_1)$	Order	Error $L_2(u_2)$	Order	$L_2(u_3)$	Order
$10 \times 10 \times 10$	4.16×10^{-3}		4.16×10^{-3}		7.47×10^{-3}	
$20 \times 20 \times 20$	1.04×10^{-3}	2.00	1.04×10^{-3}	2.00	1.58×10^{-3}	2.24
$40 \times 40 \times 40$	2.63×10^{-4}	1.98	2.64×10^{-4}	1.98	3.92×10^{-4}	2.01
$80 \times 80 \times 80$	6.82×10^{-5}	1.95	7.07×10^{-5}	1.90	1.00×10^{-4}	1.97

4.1.2. Position dependent shear modulus

Spatially varying shear modulus occurs frequently in natural and man-made materials and devices. The ability to deal with position-dependent material parameters cannot be overemphasized for practical applications. For example, the protein molecules can have variable shear modulus [27]. In this subsection, we consider that the shear modulus is given as a position-dependent function.

Example 7. In this example, we consider the problem defined in Example 1, while replace the shear modulus in Example 1 by the following position-dependent function

$$\mu = \begin{cases} \mu^+ = 1\,500\,000 + (x + y + z), & \text{in } \Omega^+, \\ \mu^- = 2\,000\,000 + xyz, & \text{in } \Omega^-. \end{cases}$$

The error analysis is given in Tables 31 and 32 for L_∞ and L_2 , respectively. Essentially, second order convergence is obtained. The level of accuracy is the same as that obtained for Example 1, which indicates that the proposed MIB method is robust for position-dependent material parameters.

Example 8. To further test the proposed method for its performance in dealing with variable material parameters, we consider an example by setting the shear modulus in Example 4 to the following spatially dependent functions

$$\mu = \begin{cases} \mu^+ = 1\,500\,000 + 2000(x + y + z), & \text{in } \Omega^+, \\ \mu^- = 2\,000\,000 + 1500xyz, & \text{in } \Omega^-. \end{cases}$$

The L_∞ and L_2 errors are analyzed in Tables 33 and 34, respectively.

Example 9. In this numerical experiment, we further investigate the robustness of the proposed MIB algorithm to the position dependent shear modulus, now we redo Example 8, however, change the shear modulus in Example 8 to be the following functions:

$$\mu = \begin{cases} \mu^+ = 1\,500\,000 + 2000(x^2 + y^2 + z^2), & \text{in } \Omega^+, \\ \mu^- = 2\,000\,000 + 1500x^2y^2z^2, & \text{in } \Omega^-. \end{cases}$$

Table 35
The L_∞ errors of Example 9.

Grid size	$L_\infty(u_1)$	Order	$L_\infty(u_2)$	Order	$L_\infty(u_3)$	Order
$20 \times 20 \times 20$	1.67×10^{-1}		1.65×10^{-1}		9.39×10^{-2}	
$40 \times 40 \times 40$	4.20×10^{-2}	1.99	5.36×10^{-2}	1.62	2.66×10^{-2}	1.82
$80 \times 80 \times 80$	9.97×10^{-3}	2.07	9.71×10^{-3}	2.48	5.96×10^{-3}	2.43

Table 36
The L_2 errors of Example 9.

Grid size	$L_2(u_1)$	Order	Error $L_2(u_2)$	Order	$L_2(u_3)$	Order
$20 \times 20 \times 20$	4.27×10^{-2}		4.26×10^{-2}		1.78×10^{-2}	
$40 \times 40 \times 40$	1.10×10^{-2}	1.96	1.09×10^{-2}	1.97	4.48×10^{-3}	1.99
$80 \times 80 \times 80$	2.80×10^{-3}	1.97	2.78×10^{-3}	1.97	1.08×10^{-3}	2.05

Table 37
The L_∞ errors of Example 10.

Grid size	$L_\infty(u_1)$	Order	$L_\infty(u_2)$	Order	$L_\infty(u_3)$	Order
0.6	5.08×10^{-2}		5.18×10^{-2}		6.60×10^{-2}	
0.3	1.39×10^{-2}	1.87	1.41×10^{-2}	2.06	1.74×10^{-2}	1.92
0.15	3.07×10^{-3}	2.18	3.77×10^{-3}	2.18	4.09×10^{-3}	2.09

The L_∞ and L_2 errors are analyzed in Tables 35 and 36, respectively.

Remark 5. From the above three examples, we observe the second order accuracy in both L_∞ and L_2 norms for elasticity interfaces with position-dependent material parameters. Additionally the level of accuracy is not affected by the spatially varying material parameters.

4.2. Nonsmooth interfaces

Nonsmooth interfaces are omnipresent in practical applications and give rise to challenges for numerical algorithm design. In this section, we consider a few elasticity interface problems with geometric singularities.

Example 10. In this example, let us consider an apple-like interface [33]

$$\rho = 1.9(1 - \cos \phi),$$

where $\rho = \sqrt{x^2 + y^2 + z^2}$ and $\phi = \arccos \frac{z}{\rho}$. The computational domain is set to $[-5, 4.6] \times [-5, 4.6] \times [-8, 4]$.

The values of the Poisson’s ratio and shear modulus are, respectively

$$v = \begin{cases} v^+ = 0.24, & \text{in } \Omega^+, \\ v^- = 0.20, & \text{in } \Omega^- \end{cases}$$

and

$$\mu = \begin{cases} \mu^+ = 2\,000\,000, & \text{in } \Omega^+, \\ \mu^- = 1\,500\,000, & \text{in } \Omega^-. \end{cases}$$

The Dirichlet boundary condition and interface jump conditions can be determined by the following exact solution

$$u_1(x, y, z) = \begin{cases} \cos x \cos y \cos z + xyz, & \text{in } \Omega^+, \\ 3, & \text{in } \Omega^-, \end{cases}$$

$$u_2(x, y, z) = \begin{cases} \cos x \cos y \cos z + x^2 + y^2 + z^2, & \text{in } \Omega^+, \\ 3, & \text{in } \Omega^-, \end{cases}$$

and

$$u_3(x, y, z) = \begin{cases} \cos x \cos y \cos z, & \text{in } \Omega^+, \\ 3, & \text{in } \Omega^-. \end{cases}$$

Grid refinement analysis in terms of L_∞ error is given in Table 37. A similar L_2 error analysis is given in Table 38. The level of accuracy and the order of convergence are similar to those observed in earlier cases.

Figs. 19 and 20 illustrate the numerical solution and error of solving the apple-like interface problem with grid size 0.15. The grid refinement analysis in Table 37 and Table 38 indicate the second order convergence in both L_2 and L_∞ error

Table 38
The L_2 errors of Example 10.

Grid size	$L_2(u_1)$	Order	Error $L_2(u_2)$	Order	$L_2(u_3)$	Order
0.6	5.86×10^{-3}		6.11×10^{-3}		9.44×10^{-3}	
0.3	1.51×10^{-3}	2.17	1.61×10^{-3}	1.92	2.55×10^{-3}	1.89
0.15	3.77×10^{-4}	2.07	3.96×10^{-4}	2.02	6.69×10^{-4}	1.93

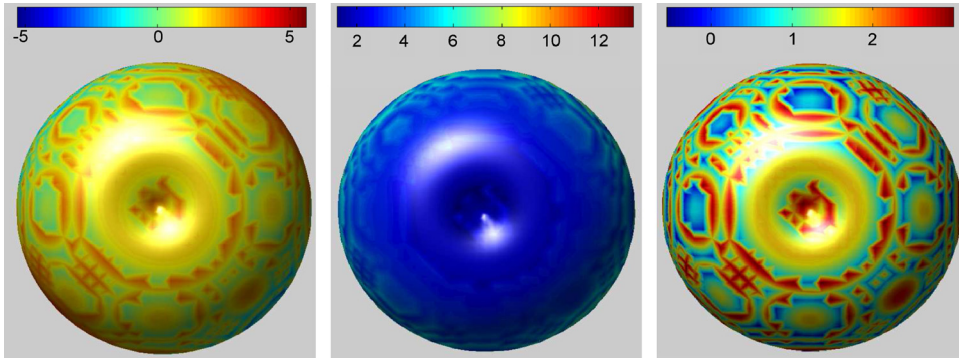


Fig. 19. Solution to the apple-like interface problem with grid size 0.15. Left chart: u_1 ; Middle chart: u_2 ; Right chart: u_3 .

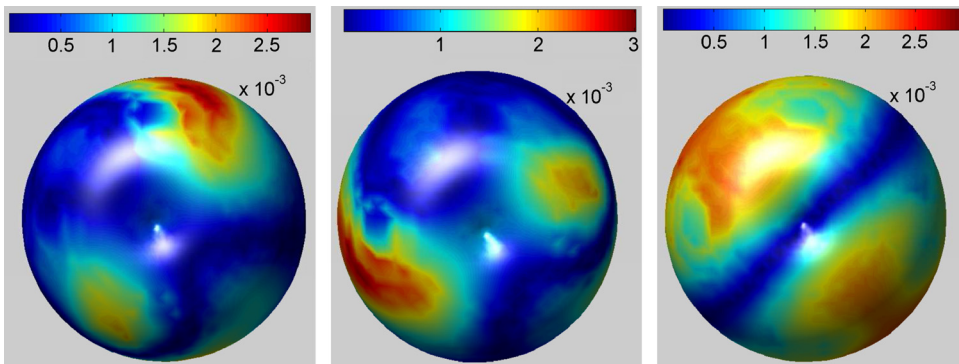


Fig. 20. Numerical error for solving the apple-life interface problem with grid size 0.15. Left chart: u_1 ; Middle chart: u_2 ; Right chart: u_3 .

Table 39
The L_∞ errors of Example 11.

Grid size	$L_\infty(u_1)$	Order	$L_\infty(u_2)$	Order	$L_\infty(u_3)$	Order
0.48	3.90×10^{-2}		4.28×10^{-2}		6.18×10^{-2}	
0.24	9.92×10^{-3}	1.98	1.01×10^{-2}	2.08	1.19×10^{-2}	2.38
0.12	2.29×10^{-3}	2.12	2.54×10^{-3}	1.99	2.60×10^{-3}	2.19

norms. Note that largest error did not occur at the geometric singularity, which indicates that the proposed MIB method works well for geometric singularities.

Example 11. Next, we consider an oak-acorn interface geometry [33]

$$\begin{cases} (\frac{x}{d})^2 + (\frac{y}{d})^2 = (z - q)^2, & \text{if } z > 0, \\ x^2 + y^2 + (z - g)^2 = R^2, & \text{if } z \leq 0, \end{cases}$$

where $q = -\frac{6}{7}$, $g = \frac{1}{2}$, $R = \frac{15}{7}$ and $d = \sqrt{\frac{R^2 - g^2}{q^2}}$. The computational domain is set to $[-5, 4.6] \times [-5, 4.6] \times [-5, 4.6]$. Note that this interface has a tip.

The material parameters and exact solutions in Example 10 are adopted. Grid refinement analysis in terms of L_∞ error is given in Table 39. In Table 40, similar analysis in terms of L_2 error is also given. These results show that the second order convergence in both L_2 and L_∞ error norms is achieved.

Table 40
The L_2 errors of Example 11.

Grid size	$L_2(u_1)$	Order	Error $L_2(u_2)$	Order	$L_2(u_3)$	Order
0.48	5.91×10^{-3}		6.37×10^{-3}		7.44×10^{-3}	
0.24	1.36×10^{-3}	2.17	1.48×10^{-3}	2.11	1.88×10^{-3}	1.98
0.12	3.25×10^{-4}	2.07	3.60×10^{-4}	2.04	4.06×10^{-4}	2.21

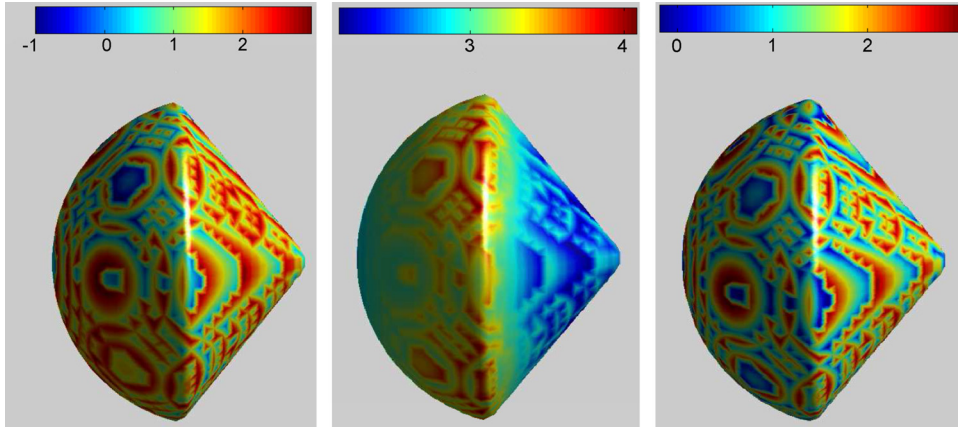


Fig. 21. Numerical solution to the acorn interface problem with grid size 0.12. Left chart: u_1 ; Middle chart: u_2 ; Right chart: u_3 .

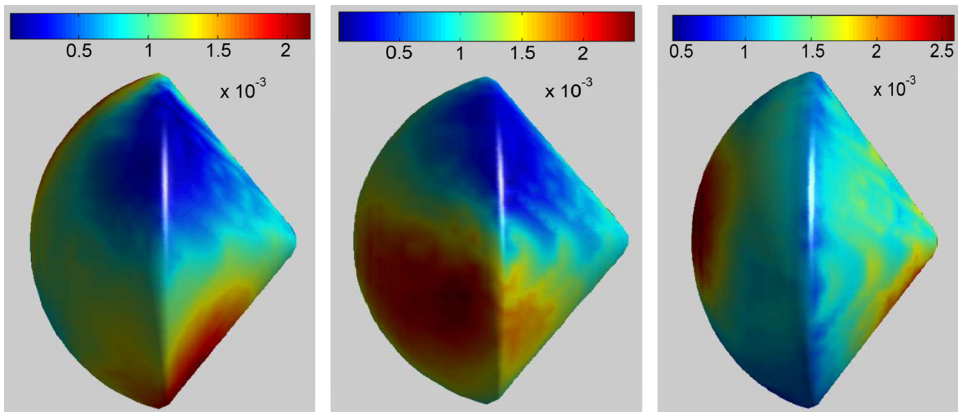


Fig. 22. Numerical error for solving the acorn interface problem with grid size 0.12. Left chart: u_1 ; Middle chart: u_2 ; Right chart: u_3 .

The geometry, numerical solution and error distribution are provided in Figs. 21 and 22, which are computed with grid size 0.15 in all directions. Again, the largest error is away from the tip, which indicates the robustness of the present MIB method for dealing with geometric singularity.

Example 12. Finally, let us extend the benchmark pentagon-star interface test used in 2D to a 3D one, which is a more complicated interface with very a sharp edge. We set the interface as

$$\phi(r, \theta) = \begin{cases} \frac{R \sin(\theta_t/2)}{\sin(\theta_t/2 + \theta - \theta_r - 2\pi(i-1)/5)} - r, & \theta_r + \pi(2i - 2)/5 \leq \theta < \theta_r + \pi(2i - 1)/5, \\ \frac{R \sin(\theta_t/2)}{\sin(\theta_t/2 - \theta + \theta_r + 2\pi(i-1)/5)} - r, & \theta_r + \pi(2i - 3)/5 \leq \theta < \theta_r + \pi(2i - 2)/5, \end{cases}$$

where $\theta_t = \frac{\pi}{5}$, $\theta_r = \frac{\pi}{7}$, $R = \frac{6}{7}$ and $i = 1, 2, 3, 4, 5$. Furthermore, we have $r = \sqrt{x^2 + y^2}$ and $\theta = \arctan \frac{y}{x}$. The z -direction of the interface is constrained by

$$-\frac{\sqrt{3}}{2} \leq z \leq \frac{\sqrt{3}}{2}.$$

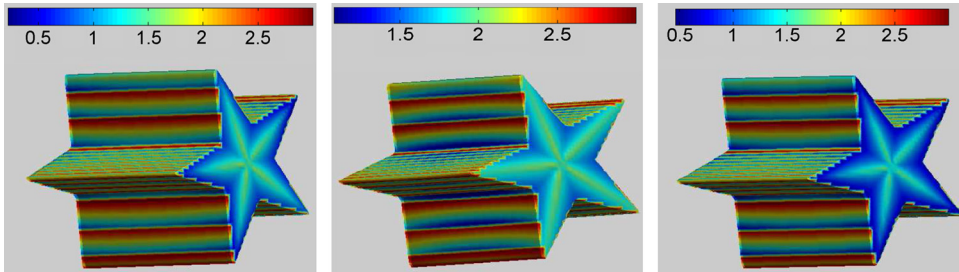
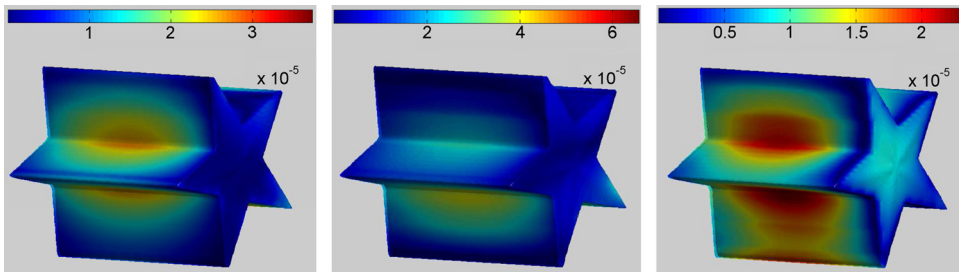
The computational domain is set to $[-1.3, 1.1] \times [-1.3, 1.1] \times [-1.3, 1.1]$. The material parameters and exact solutions in Example 10 are utilized for this problem.

Table 41The L_∞ errors of Example 12.

Grid size	$L_\infty(u_1)$	Order	$L_\infty(u_2)$	Order	$L_\infty(u_3)$	Order
0.12	1.27×10^{-3}		1.57×10^{-3}		1.75×10^{-2}	
0.06	2.08×10^{-4}	2.61	3.98×10^{-4}	1.98	1.76×10^{-4}	3.31
0.03	3.80×10^{-5}	2.45	6.56×10^{-5}	2.60	2.79×10^{-5}	2.66

Table 42The L_2 errors of Example 12.

Grid size	$L_2(u_1)$	Order	Error $L_2(u_2)$	Order	$L_2(u_3)$	Order
0.12	3.71×10^{-4}		1.67×10^{-4}		3.57×10^{-4}	
0.06	3.79×10^{-5}	3.29	4.47×10^{-5}	1.90	3.76×10^{-5}	3.25
0.03	7.67×10^{-6}	2.30	1.07×10^{-5}	2.60	6.08×10^{-6}	2.63

**Fig. 23.** Numerical solution to the pentagon star interface problem with grid size 0.03. Left chart: u_1 ; Middle chart: u_2 ; Right chart: u_3 .**Fig. 24.** Numerical error for solving the pentagon star interface problem with grid size 0.03. Left chart: u_1 ; Middle chart: u_2 ; Right chart: u_3 .

Grid refinement L_∞ error analysis is given in Table 41. We also shown the grid refinement analysis in terms of L_2 error in Table 42. The grid refinement analysis shows that the second order convergence in both L_2 and L_∞ error norms is obtained.

To give a visualization of the numerical solution, error and interface geometry of the pentagon star liked interface problem, we provide Figs. 23 and 24, which are plotted with grid size 0.03. In general, error is very small. Additionally, the largest error does not occur at the sharp edge of the interface. Therefore, from the above three test examples, we can conclude that the proposed MIB method is very robust in handling geometric singularities.

4.3. Biomolecular surfaces

Finally, to further test the convergence and robustness of our method, we consider a much more complex system, the molecular surface of proteins whose coordinates are obtained from the Protein Data Bank (PDB). Here we only provide the test results for two biomolecular surfaces (PDB ID: 1ptq and 1r69). To obtain an all-atom model for a protein, all attached water molecules are cleaned and hydrogen atoms are added. Atomic van der Waals radii defining the dielectric boundary were taken from the CHARMM22 force field, and the MSMS software package is utilized for the molecular surface generation. A major challenge for these surfaces is the tips and cups in the molecular surface definition. To our best knowledge, there is no other method in the literature that can deliver second order convergence for this class of problems.

Example 13. In this example, the Poisson ratio and shear modulus are set, respectively, to be:

$$\nu = \begin{cases} \nu^+ = 0.20, & \text{in } \Omega^+, \\ \nu^- = 0.24, & \text{in } \Omega^-, \end{cases}$$

Table 43
The L_∞ errors of Case 1 of Example 13.

Grid size (Å)	$L_\infty(u1)$	Order	$L_\infty(u2)$	Order	$L_\infty(u3)$	Order
1.0	2.94×10^{-1}		3.50×10^{-1}		3.72×10^{-1}	
0.5	7.21×10^{-2}	2.03	7.15×10^{-2}	2.29	1.02×10^{-1}	1.87
0.25	1.45×10^{-2}	2.31	1.48×10^{-2}	2.27	1.24×10^{-2}	3.04

Table 44
The L_2 errors of Case 1 of Example 13.

Grid size (Å)	$L_2(u1)$	Order	$L_2(u2)$	Order	$L_2(u3)$	Order
1.0	3.54×10^{-2}		2.92×10^{-2}		2.84×10^{-2}	
0.5	6.83×10^{-3}	2.37	7.88×10^{-3}	1.89	5.90×10^{-3}	2.27
0.25	1.83×10^{-3}	1.90	1.88×10^{-3}	2.07	1.32×10^{-3}	2.16

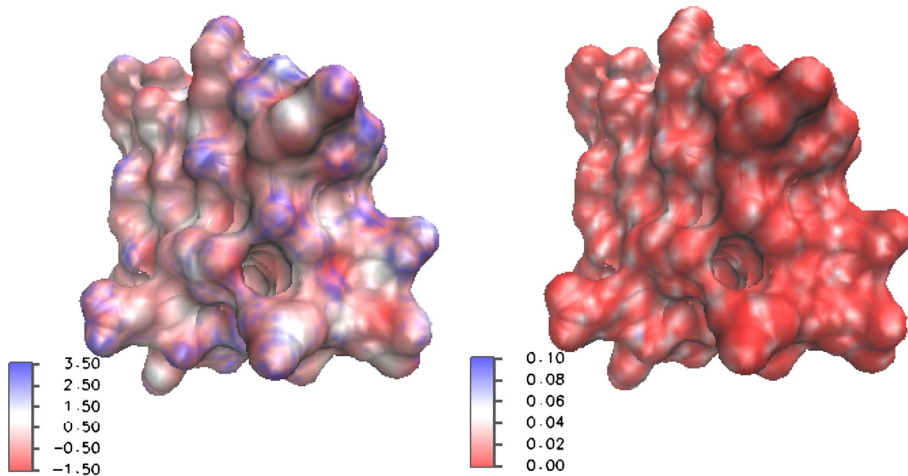


Fig. 25. The left chart shows the surface maps of the numerical solution, the surface map of the numerical error is depicted in the right chart (grid size 0.25 Å).

and

$$\mu = \begin{cases} \mu^+ = 1\,500\,000, & \text{in } \Omega^+, \\ \mu^- = 2\,000\,000, & \text{in } \Omega^-. \end{cases}$$

The Dirichlet boundary condition and interface conditions are determined from the following designed exact solutions:

$$u_1(x, y, z) = u_2(x, y, z) = u_3(x, y, z) = \begin{cases} 3, & \text{in } \Omega^+, \\ \cos(x) \cos(y) \cos(z), & \text{in } \Omega^-. \end{cases}$$

The computational domain for both of the following cases are set to be the bounding boxes of the MSMS surfaces of the protein molecules with an extra 4 Å along each side. Here Ω^+ is the subdomain that outside the MSMS surface while Ω^- is that inside the MSMS surface.

Case 1. In the first case, let the interface to be the molecular surface of the protein with PDB ID: 1ptq.

Grid refinement analysis in terms of L_∞ error is given in Table 43. In Table 44, similar analysis in terms of L_2 error is also given. The design second accuracy is achieved.

Fig. 25 shows the error and numerical solution of u_1 for Case 1 in Example 13.

Case 2. In the second case, The interface is set to be the molecular surface of the protein with PDB ID: 1r69. Grid refinement analysis in terms of L_∞ error is given in Table 45. In Table 46, similar analysis in terms of L_2 error is also given. Clearly, the proposed method achieve the second order convergence for both protein interfaces.

Fig. 26 shows the error and the numerical solution of u_1 for Case 2 in Example 13.

5. Conclusion

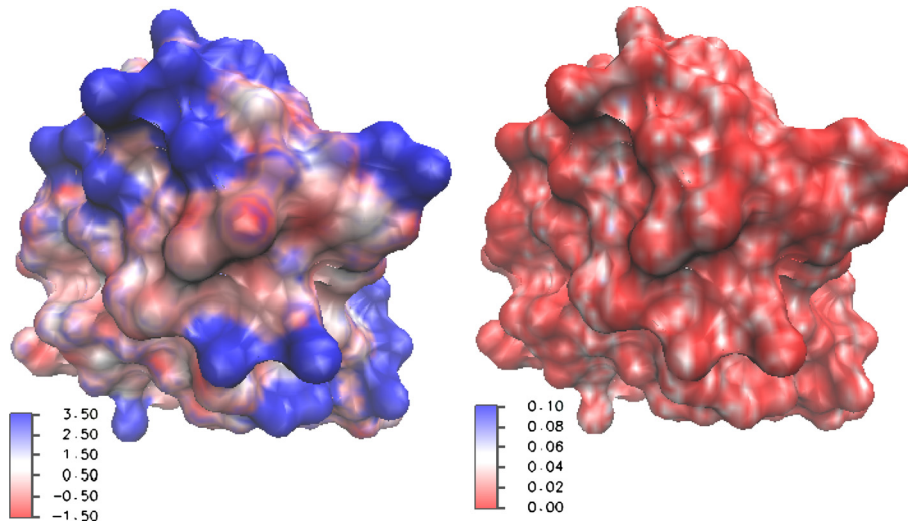
In this work, we develop the matched interface and boundary (MIB) method for solving three-dimensional (3D) elasticity interface problems. Both isotropic homogeneous material and isotropic inhomogeneous material are considered in

Table 45The L_∞ errors of Case 2 of Example 13.

Grid size (Å)	$L_\infty(u1)$	Order	$L_\infty(u2)$	Order	$L_\infty(u3)$	Order
1.0	3.23×10^{-1}		4.81×10^{-1}		4.11×10^{-1}	
0.5	1.09×10^{-1}	1.57	6.04×10^{-2}	2.99	1.26×10^{-1}	1.71
0.25	2.00×10^{-2}	2.45	1.46×10^{-2}	2.05	1.71×10^{-2}	2.88

Table 46The L_2 errors of Case 2 of Example 13.

Grid size (Å)	$L_2(u1)$	Order	$L_2(u2)$	Order	$L_2(u3)$	Order
1.0	2.97×10^{-2}		2.60×10^{-2}		2.73×10^{-2}	
0.5	8.18×10^{-3}	1.86	8.05×10^{-3}	1.70	4.94×10^{-3}	2.47
0.25	2.14×10^{-3}	1.93	1.89×10^{-3}	2.09	1.23×10^{-3}	2.01

**Fig. 26.** The left chart depicts the surface maps of the numerical solution, the surface map of the numerical error is illustrated in the right chart (grid size 0.25 Å).

the theoretical modeling and numerical computation. In particular, the isotropic inhomogeneous material is described by a strain-stress constitutive law with a position-dependent modulus function.

Most previous effort in the MIB method has been for elliptic interface problems. Its essential idea is to replace function values on irregular grid points fictitious values in the discretization so that the standard finite difference schemes can be systematically employed as if there were no interface. Interface jump conditions are enforced on the intersecting points between the interface and the mesh lines, which in turn determines fictitious values. In principle, the MIB method developed for one interface problem can be utilized for solving another interface problem because the MIB procedure does depend on the form of the partial differential equation. However, elasticity interface equations are exceptional because they involve both central derivatives and cross derivatives, which lead to new difficulties in determining fictitious values. Additionally, the elasticity interface equation is a vector equation with three deformation components in a 3D setting, which results in more demanding in efficient numerical schemes in terms of computer memory storage and convergent speed in solving the linear algebraic system. Consequently, a new MIB algorithm has been developed in this work to address these issues. To make the MIB scheme of second order convergence, a number of new techniques for central derivatives and cross derivatives is proposed in this work. For central derivatives, techniques such as local coordinate transformation, disassociation, two sets of jump conditions are utilized, while for cross derivatives, disassociation, extrapolation and neighbor combination techniques are proposed to determining fictitious values. The resulting large sparse linear systems for the coupled vector equations are solved efficiently by using the bi-conjugated gradient method.

The proposed new MIB scheme has been validated by using a variety of benchmark examples. In terms of interface complexity, we considered both smooth interfaces and nonsmooth interfaces as well protein interfaces. Smooth interface geometries include sphere, hemisphere, genus-1 torus, flower and cylinder. In the category of nonsmooth interface geometries, apple-shaped, oak-acorn-shaped and pentagon star interfaces are considered. It is well known that in order to achieve second order convergence, nonsmooth interface geometries require special considerations in the interface algorithm design. The robustness of the MIB method proved by showing that the largest error occurs away from the geometric singularities.

The proposed new MIB scheme has also been tested for elasticity interface problems with both weak discontinuity and strong discontinuity in solutions. Another standard test is the stability of the numerical schemes for large contrasts in material parameters across the interface. These aspects are investigated with numerous examples. We have demonstrated that the proposed MIB method is not sensitive to change in discontinuity and material contrast.

Finally, two classes of material parameters, namely, piecewise constants and spatially varying Poisson's ratio and shear modulus are considered in our numerical experiments. We have demonstrated with extensive numerical examples that proposed MIB method achieve second order convergence in both L_∞ and L_2 error norms for all the tests described above. Additionally, the level of MIB accuracy is not affected the above mentioned test issues. The present test on complex biomolecular systems indicates that the present MIB scheme is ready for applications to the real world elastic problems. To our best knowledge, there is no other elasticity interface method in the literature that can achieve the second order convergence for arbitrarily complex biomolecular interfaces.

Acknowledgements

This work was supported in part by NSF grants IIS-1302285 and DMS-1160352, NIH grant R01GM-090208 and MSU Center for Mathematical Molecular Biosciences Initiative.

References

- [1] A. Anandarajah, *Computational Methods in Elasticity and Plasticity: Solids and Porous Media*, Springer, 2010.
- [2] R. Becker, E. Burman, P. Hansbo, A Nitsche extended finite element method for incompressible elasticity with discontinuous modulus of elasticity, *Comput. Methods Appl. Mech. Eng.* 198 (2009) 3352–3360.
- [3] D. Chen, Z. Chen, C. Chen, W.H. Geng, G.W. Wei, MIBPB: a software package for electrostatic analysis, *J. Comput. Chem.* 32 (2011) 657–670.
- [4] Z. Chen, N.A. Baker, G.W. Wei, Differential geometry based solvation models I: Eulerian formulation, *J. Comput. Phys.* 229 (2010) 8231–8258.
- [5] G. Dvorak, *Micromechanics of Composite Materials*, Springer, 2013.
- [6] J.D. Eshelby, The continuum theory of lattice defects, *Prog. Solid State Phys.* 3 (1956) 79–144.
- [7] J.D. Eshelby, The determination of the elastic field of an ellipsoidal inclusion, and related problems, *Proc. R. Soc. Lond. Ser. A, Math. Phys. Sci.* 241 (1957) 376–396.
- [8] B. Fornberg, Calculation of weights in finite difference formulas, *SIAM Rev.* 40 (1998) 685–691.
- [9] T.P. Fries, T. Belytschko, The extended/generalized finite element method: an overview of the method and its applications, *Int. J. Numer. Methods Eng.* 84 (2010) 253–304.
- [10] W. Geng, G.W. Wei, Multiscale molecular dynamics using the matched interface and boundary method, *J. Comput. Phys.* 230 (2) (2011) 435–457.
- [11] W. Geng, S. Yu, G.W. Wei, Treatment of charge singularities in implicit solvent models, *J. Chem. Phys.* 127 (2007) 114106.
- [12] A. Hansbo, P. Hansbo, An unfitted finite element method, *Comput. Methods Appl. Mech. Eng.* 191 (2002) 5537–5552.
- [13] S. Hou, Z. Li, L. Wang, W. Wang, A numerical method for solving elasticity equations with sharp-edged interfaces, *Commun. Comput. Phys.* 12 (2012) 595–612.
- [14] R.J. LeVeque, Z.L. Li, The immersed interface method for elliptic equations with discontinuous coefficients and singular sources, *SIAM J. Numer. Anal.* 31 (1994) 1019–1044.
- [15] Z.L. Li, X.Z. Yang, An immersed fem for elasticity equations with interfaces, *Contemp. Math.* 383 (2005) 285–298.
- [16] T. Lin, D.W. Sheen, X. Zhang, A locking-free immersed finite element method for planar elasticity interface problems, *J. Comput. Phys.* 247 (2013) 228–247.
- [17] T. Lin, X. Zhang, Linear and bilinear immersed finite elements for planar elasticity interface problems, *J. Comput. Appl. Math.* 236 (2012) 4681–4699.
- [18] J. Mathiesen, I. Procaccia, I. Regev, Elasticity with arbitrarily shaped inhomogeneity, *Phys. Rev. E* 77 (2008) 026606.
- [19] J. Mergheim, *Computational modeling of strong and weak discontinuities*, PhD thesis, Technical University of Kaiserslautern, 2006.
- [20] M. Michaeli, F. Assous, A. Golubchik, A Nitsche type method for stress fields calculation in dissimilar material with interface crack, *Appl. Numer. Math.* 67 (2013) 187–203.
- [21] P.M. Shearer, *Introduction to Seismology*, Cambridge University Press, 1999.
- [22] M. Stolarska, D.L. Chopp, N. Moes, T. Belytschko, Modelling crack growth by level sets in the extended finite element method, *Int. J. Numer. Methods Eng.* 51 (2001) 943–960.
- [23] N. Sukumar, D.L. Chopp, N. Moes, T. Belytschko, Modeling holes and inclusions by level sets in the extended finite-element method, *Comput. Methods Appl. Mech. Eng.* 190 (2001) 6180–6200.
- [24] M. Theillard, L.F. Djodjod, J.L. Vie, F. Gibou, A second-order sharp numerical method for solving the linear elasticity equations on irregular domains and adaptive grids – application to shape optimization, *J. Comput. Phys.* 233 (2013) 430–448.
- [25] G.W. Wei, Differential geometry based multiscale models, *Bull. Math. Biol.* 72 (2010) 1562–1622.
- [26] G.-W. Wei, Multiscale, multiphysics and multidomain models I: basic theory, *J. Theor. Comput. Chem.* 12 (8) (2013) 1341006.
- [27] K.L. Xia, K. Opron, G.W. Wei, Multiscale multiphysics and multidomain models – flexibility and rigidity, *J. Chem. Phys.* 139 (2013) 194109.
- [28] K.L. Xia, M. Zhan, G.-W. Wei, The matched interface and boundary (MIB) method for multi-domain elliptic interface problems, *J. Comput. Phys.* 230 (2011) 8231–8258.
- [29] H. Xie, Z.L. Li, Z.H. Qiao, A finite element method for elasticity interface problems with locally modified triangulations, *Int. J. Numer. Anal. Model.* 8 (2011) 189–200.
- [30] Z.L. Xu, J. Glimm, X.L. Li, Front tracking algorithm using adaptively refined meshes, in: *Adaptive Mesh Refinement – Theory and Applications*, in: *Lecture Notes in Computational Science and Engineering*, September 2003, pp. 83–89.
- [31] X.Z. Yang, B. Li, Z.L. Li, The immersed interface method for elasticity problems with interface, *Dyn. Contin. Discrete Impuls. Syst. Ser. A Math. Anal.* 10 (2003) 783–808.
- [32] S.N. Yu, W.H. Geng, G.W. Wei, Treatment of geometric singularities in implicit solvent models, *J. Chem. Phys.* 126 (2007) 244108.
- [33] S.N. Yu, G.W. Wei, Three-dimensional matched interface and boundary (MIB) method for treating geometric singularities, *J. Comput. Phys.* 227 (2007) 602–632.
- [34] S. Zhao, Full-vectorial matched interface and boundary (MIB) method for the modal analysis of dielectric waveguides, *J. Lightwave Technol.* 26 (2008) 2251–2259.
- [35] S. Zhao, High order matched interface and boundary methods for the Helmholtz equation in media with arbitrarily curved interfaces, *J. Comput. Phys.* 229 (2010) 3155–3170.

- [36] S. Zhao, G.W. Wei, High-order FDTD methods via derivative matching for Maxwell's equations with material interfaces, *J. Comput. Phys.* 200 (1) (2004) 60–103.
- [37] Q. Zheng, D. Chen, G.W. Wei, Second-order Poisson–Nernst–Planck solver for ion transport, *J. Comput. Phys.* 230 (2011) 5239–5262.
- [38] Q. Zheng, G.W. Wei, Poisson–Boltzmann–Nernst–Planck model, *J. Chem. Phys.* 134 (2011) 194101.
- [39] Y.C. Zhou, M. Feig, G.W. Wei, Highly accurate biomolecular electrostatics in continuum dielectric environments, *J. Comput. Chem.* 29 (2008) 87–97.
- [40] Y.C. Zhou, J.G. Liu, D.L. Harry, A matched interface and boundary method for solving multi-flow Navier–Stokes equations with applications to geodynamics, *J. Comput. Phys.* 231 (2012) 223–242.
- [41] Y.C. Zhou, G.W. Wei, On the fictitious-domain and interpolation formulations of the matched interface and boundary (MIB) method, *J. Comput. Phys.* 219 (1) (2006) 228–246.
- [42] Y.C. Zhou, S. Zhao, M. Feig, G.W. Wei, High order matched interface and boundary method for elliptic equations with discontinuous coefficients and singular sources, *J. Comput. Phys.* 213 (1) (2006) 1–30.